

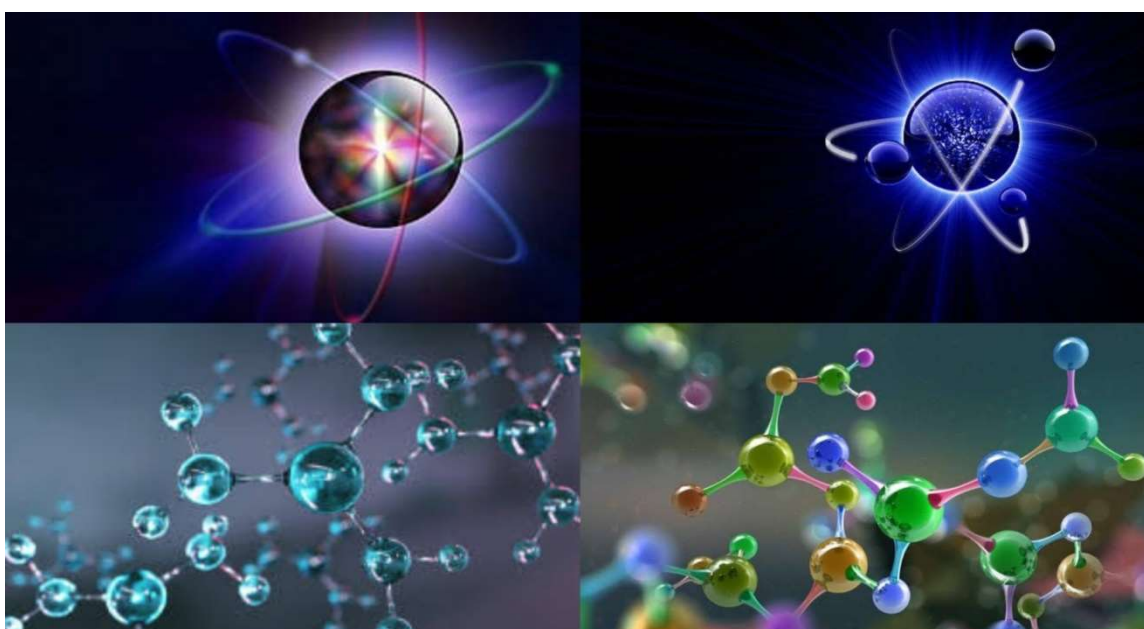


ISSN : 2830-8085

DOI : <https://doi.org/10.58452/jpcr.v2i2>

Journal of Physical & Chemical Research

Volume 2, Issue 2, December (2023) 1-80



Pr. Kahoul Abdelhalim
Editor-in-Chief

First Legal Deposit: December, 2023

Journal homepage: <https://ojs.univ-bba.dz>

Journal of Physical and Chemical Research

- **Honorary Director:**
Pr. Bouazza Boudersaya
Rector of Mohamed El Bachir El Ibrahimi University, Bordj-Bou-Argeridj, Algeria
- **Director :**
Pr. Kahoul Abdelhalim
Head of Laboratory of Materials Physics, Radiation and Nanostructures(LPMRN)
- **Editor-in-Chief:**
Pr. Kahoul Abdelhalim
a.kahoul@univ-bba.dz; ahalim.kahoul@gmail.com
Mohamed El Bachir El Ibrahimi University, Bordj-Bou-Argeridj, Algeria.
- **Associate Editors:**
 - In Physical Research**
 - Khalfallah Farid
f.khalfallah@univ-bba.dz ; khal.far@gmail.com
Mohamed El Bachir El Ibrahimi University, Bordj-Bou-Argeridj, Algeria.
 - Daoudi Salim
s.daoudi@univ-bba.dz ; salzdg@gmail.com
Mohamed El Bachir El Ibrahimi University, Bordj-Bou-Argeridj, Algeria.
 - Sahnoune Yassine
yassine.sahnoune@univ-bba.dz ; sahnoun.y34@gmail.com
Mohamed El Bachir El Ibrahimi University, Bordj-Bou-Argeridj, Algeria.
 - In Chemical Research**
 - Khelladi Mohamed Ridha
mohamedridha.khelladi@univ-bba.dz ; redha2022@yahoo.fr
Mohamed El Bachir El Ibrahimi University, Bordj-Bou-Argeridj, Algeria.
 - Tabti Salima
salima.tabti@univ-bba.dz ; thabti_sa@yahoo.fr
Mohamed El Bachir El Ibrahimi University, Bordj-Bou-Argeridj, Algeria.
 - Chikouche Imene
imene.chikouche@univ-bba.dz ; chikouche_imene@yahoo.fr
Mohamed El Bachir El Ibrahimi University, Bordj-Bou-Argeridj, Algeria.
- **Secretariat**
 - Hama Amel
amel.hama@univ-bba.dz
Mohamed El Bachir El Ibrahimi University, Bordj-Bou-Argeridj, Algeria.
 - Akmoum Khemisti
khemisti.akmoum@univ-bba.dz
Mohamed El Bachir El Ibrahimi University, Bordj-Bou-Argeridj, Algeria.
 - Benchiheb Nadjat
nadjat.benchiheb@univ-bba.dz
Mohamed El Bachir El Ibrahimi University, Bordj-Bou-Argeridj, Algeria.
 - Messaoudi Yazid
Messaoudi.yazid@univ-setif.dz
Ferhat Abbas University -Sétif 1-, Algeria.

- **Scientific committee**
- Laraoui Abdelghani
alaraqoui2@unl.edu
Department of Mechanical & Materials Engineering, University of Nebraska – Lincoln, USA.
- Nuray Kup Aylikci
nuray.aylikci@iste.edu.tr
Department of Energy Systems Engineering, Faculty of Engineering and Natural Sciences.
Iskenderun Technical University, Iskenderun, Hatay, Turkey.
- Volkan Aylikci
volkan.aylikci@iste.edu.tr
Department of Metallurgical and Materials Engineering,
Faculty of Engineering and Natural Sciences, Iskenderun Technical University,
Iskenderun, Hatay, Turkey.
- Sarra Mustapha
sarramust1@yahoo.fr
Mohamed El Bachir El Ibrahimi University, Bordj-Bou-Arreridj, Algeria.
- Latrache Abdelhakim
abdelhakim.latreche@univ-bba.dz
Mohamed El Bachir El Ibrahimi University, Bordj-Bou-Arreridj, Algeria.
- Abdelhalim Bencheikh
abdelhalim.bencheikh@univ-bba.dz
Mohamed El Bachir El Ibrahimi University, Bordj-Bou-Arreridj, Algeria.
- Bentabet Abdelouahab
abdelouahab.bentabet@univ-bba.dz
Mohamed El Bachir El Ibrahimi University, Bordj-Bou-Arreridj, Algeria
- Lebgaa Nodjoud
noudjoud.lebga@univ-bba.dz
Mohamed El Bachir El Ibrahimi University, Bordj-Bou-Arreridj, Algeria.
- Bahloul Ahmed
ahmed.bahloul@univ-bba.dz
Mohamed El Bachir El Ibrahimi University, Bordj-Bou-Arreridj, Algeria.
- Hellati Abdelhak
abdelhak.hellati@univ-bba.dz
Mohamed El Bachir El Ibrahimi University, Bordj-Bou-Arreridj, Algeria.
- Boufassa Samia
samia.boufassa@univ-bba.dz
Mohamed El Bachir El Ibrahimi University, Bordj-Bou-Arreridj, Algeria.
- Benamrani Ammar
ammar.benamrani@univ-bba.dz
Mohamed El Bachir El Ibrahimi University, Bordj-Bou-Arreridj, Algeria.
- Daoud Salah
salah.daoud@univ-bba.dz
Mohamed El Bachir El Ibrahimi University, Bordj-Bou-Arreridj, Algeria.
- Riad Ayache
riad.ayache@univ-bba.dz
Mohamed El Bachir El Ibrahimi University, Bordj-Bou-Arreridj, Algeria.
- Khelladi Mohamed Ridha
mohamedridha.khelladi@univ-bba.dz ; redha2022@yahoo.fr
Mohamed El Bachir El Ibrahimi University, Bordj-Bou-Arreridj, Algeria.
- Tabti Salima
salima.tabti@univ-bba.dz ; thabti_sa@yahoo.fr
Mohamed El Bachir El Ibrahimi University, Bordj-Bou-Arreridj, Algeria.

- Chikouche Imene
imene.chikouche@univ-bba.dz ; chikouche_imene@yahoo.fr
Mohamed El Bachir El Ibrahimi University, Bordj-Bou-Argeridj, Algeria.
- Khalfallah Farid
f.khalfallah@univ-bba.dz ; khal.far@gmail.com
Mohamed El Bachir El Ibrahimi University, Bordj-Bou-Argeridj, Algeria.
- Daoudi Salim
s.daoudi@univ-bba.dz ; salzdg@gmail.com
Mohamed El Bachir El Ibrahimi University, Bordj-Bou-Argeridj, Algeria.
- Sahnoune Yassine
yassine.sahnoune@univ-bba.dz ; sahnoun.y34@gmail.com
Mohamed El Bachir El Ibrahimi University, Bordj-Bou-Argeridj, Algeria.
- Bioud Nadhira
nadhira.bioud@univ-bba.dz
Mohamed El Bachir El Ibrahimi University, Bordj-Bou-Argeridj, Algeria
- Kasri Yazid
yazidkasri@yahoo.fr
University of Béjaia.
- Deghfel Bahri
badeghfel@gmail.com
University of M'sila
- Baadji Nadjib
nadjibbaadji@gmail.com
University of M'sila
- Lamiri Leila
l.lamiri@crti.dz
Unité de Développement des Couches, Minces et Applications (UDCMA-CRTI), Sétif.
- Laidoudi Samiha
s.laidoudi@crti.dz
Unité de Développement des Couches, Minces et Applications (UDCMA-CRTI), Sétif.
- Belgherbi Ouafia
o.belgherbi@crti.dz
Unité de Développement des Couches, Minces et Applications (UDCMA-CRTI), Sétif.
- Kaabi Ilhem
Kaabi.ilhem@univ-setif.dz
Ferhat Abbas University -Sétif 1-, Algeria.
- Boudour Samah
s.boudour@crti.dz
Unité de Développement des Couches Minces et Applications (UDCMA-CRTI)
- Belhadj Hamza
email: hbelhadj@cdta.dz , belhadjhamza@gmail.com
Unité de Recherche en Nanosciences et Nanotechnologies
Centre de Développement des Technologies Avancées (CDTA)
- Hamza Djamel
Email : djamel.hamza@univ-setif.dz
Département de chimie, Faculté des Sciences, Université Ferhat ABBAS- Sétif 1
- Hayette Faïd
hayettefaïd@univ-bba.dz
Mohamed El Bachir El Ibrahimi University, Bordj-Bou-Argeridj, Algeria.
- Fares Nor El Houda
norelhouda.fares@univ-bba.dz; fares_houda@yahoo.fr
Département Recherche Opérationnelle, Faculté Mathématiques et Informatiques
Mohamed El Bachir El Ibrahimi University, Bordj-Bou-Argeridj, Algeria

Physical Research

- **Techno-economic analysis of a thermodynamic solar power plant based on molten salts in different sites in Algeria**
Fatah BOUFOUDI, Sofiane MIHOUB and Salah ZOUAOU
Article p:1-8.
- **Optimal design of solar energy-based hydrogen refueling station: a case study of Touggourt, Algeria**
Ahmed Zouhir Kouache, Ahmed Djafour, Khaled Mohammed Said Benzaoui, Souheil Touili and Madjida Ramdani
Article p:9-17.
- **Evolution with temperature of point defects concentration in Fe₂ZrX (X=V, Y, Tc, Ru): DFT and Wagner-Schottky modeling**
Lyacine Rabahi, Leila Rouaiguia and Abdelhafid Kellou
Article p:18-28.
- **Contribution à l'étude du nettoyage des panneaux photovoltaïques par procédé électrostatique**
Zeid Bendaoudi, Nezha Kadous, Khelifa Yanallah, Yassine Bellebna et Amar Tilmatine
Article p:29-34.
- **Acoustic characterization of superconductor material Pr123**
N. Sayoud
Article p:35-40.
- **DFT study of the electronic and optical properties of ternary alkali metal tetrafluoridobromates materials ABrF₄ (A=Na, K and Rb)**
Ishak Mebarkia
Article p:41-49.
- **L1 sub-shell fluorescence yield for lanthanide elements with $58 \leq Z \leq 71$**
K. Meddough, A. Kahoul, S. Daoudi, J.M. Sampaio, J.P. Marques, F. Parente, A. Hamidani, N.Kup Aylikci, V. Aylikci and Y. Kasri
Article p:50-56.

Chemical Research

- **Agricultural Applications of Nanocomposites Superabsorbent Polymers: A Review**
Mohammad Alrbaihat
Article p:57-71.
- **Thermal/optical study and characterization of a MCP doped with In₂O₃ and AlCl₃ for solar use**
Maifi Lyes, Agroui Kame, Hioual Ouided and Chari Abdelhamid
Article p:72-80.



Techno-economic analysis of a thermodynamic solar power plant based on molten salts in different sites in Algeria

Fatah BOUFOUDI^{1*}, Sofiane MIHOUB² and Salah ZOUAOU¹

¹Departement of Mechanical Engineering, Mouloud Mammeri University, Tizi Ouzou, 15000, Algeria.

²Departement of Physcs, Ibn Khaldoun University, Tiaret, 14000, Algeria.

* Corresponding author: E-mail address: fatah.boufoudi@ummto.dz

DOI: <https://doi.org/10.58452/jpcr.v2i2.157>

Article history

Received April 11, 2023

Accepted for publication November 02, 2023

Abstract

The use of renewable energies is one of the solutions to reduce CO₂ in the atmosphere and to satisfy our energy needs. Because, the exploitation of fossil energies such as carbon, gas and oil are responsible for the disruption of the climate system and the considerable increase of the temperature during the year and especially during the summer season as well as the atmospheric pollution. Algeria is one of the countries that is committed to this strategy and policy. This study presents a numerical simulation of a concentrated solar power plant with Fresnel mirror solar concentrator and thermal storage system. This study is carried out in the regions of Tamanrasset, Laghouat and Mascara. The SAM (System Advisor Model) software was used to calculate the DNI (Direct Normal Irradiation) of each region, the wind speed, the nominal and real LCOE (Levelized Cost Of Electricity) and the annual water consumption of the plant. The results of this simulation show that the Tamanrasset site is better selected with the annual capacity factor (CF) was 47.2%, the annual amount of water consumed is about 38709 m³. The nominal and real (LCOE) are 14.57 €/kWh and 11.56 €/kWh, respectively.

Keywords: LCOE, Efficiency, SAM.

Special Issue of the National Seminar of physics, Chemistry and their Applications "NSPCA '23" March 6-7th, 2023, Mohamed El Bachir El Ibrahimi University, Bordj-Bou-Argeridj, Algeria.

1. Introduction

Fossil energies such as oil, gas, nuclear and coal have been considered as engines for the development of societies, especially for producing electricity and heating. Unfortunately, the exploitation of these energies without conscience by man has caused drawbacks and problems that threaten our planet, Because, man exploits all these energies as if they were inexhaustible and sustainable, among its consequences; greenhouse gas emissions, global warming, pollution, etc. At present, there is no other choice but to find sources that can replace these fossil resources and face climate problems. Renewable energies are one of the solutions that can deal with the above-mentioned problems and can replace fossil energies. Renewable energies use natural resources such as (the sun, wind, waterfalls, tides, plants earth, etc.) to convert them into other energy sources such as electricity and heat. The electrical and heating energy produced by renewable energies are classified as follows; marine energy (0.01%), solar energy (0.6%), geothermal energy (1.7%), biomass (6.3%), and wind energy (7%) [1-2-3]. Algeria is one of the countries that have thought about the dynamics of green energy and the development of renewable energy, among its objectives is to engage in a new energy strategy based on renewable and sustainable energy [4]. Algeria is considered among the countries that receive a really important potential in solar energy, due to its great Sahara whose annual average irradiation in this region is very favorable as shown in Figure 1.

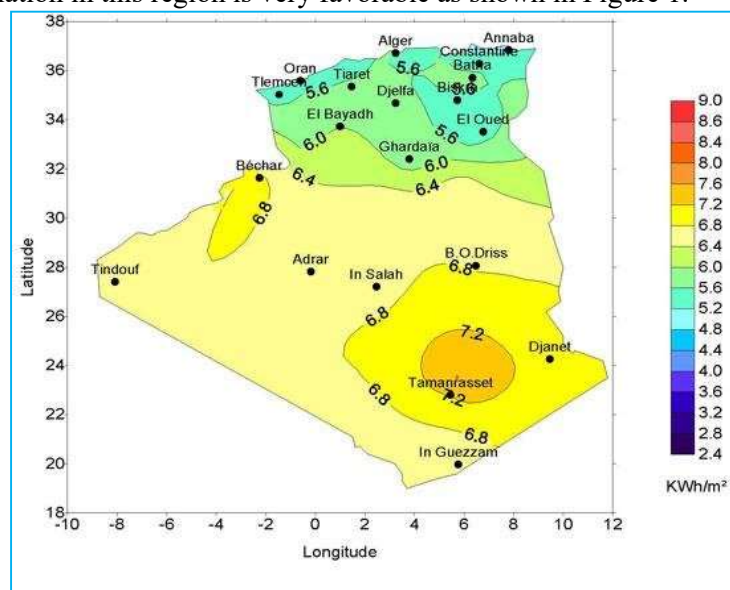


Figure 1. Global solar radiation in Algeria [5]

Special Issue of the National Seminar of physics, Chemistry and their Applications "NSPCA '23" March 6-7th, 2023, Mohamed El Bachir El Ibrahimi University, Bordj-Bou-Argeridj, Algeria.

2. Method

The plant studied is a concentrating solar power plant with Fresnel mirror, with a power of 100 MWe, its characteristics are detailed in the table below and in Figure 2.

Table 1. Characteristics of the solar power plant studied.

Style name	Brief description
Sites	Mascara,Laghouat,Mascara
Single loop aperture	8217.6 m ²
Actual number of loops	53
Field inlet temperature	230°C
Field outlet temperature	440°C
Fossil fill fraction	0
Condenser type	Air-cooled
Storage HTF	Hitec Solar Salt
Thermal Storage	4h

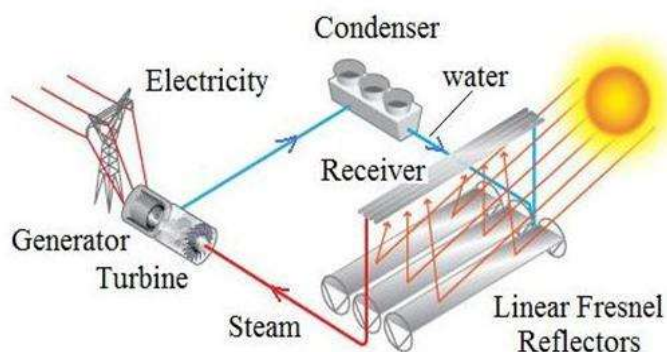


Figure 2. Solar power plant with Fresnel collector.

2.1 Mathematical models

Most models are based on the energy balance of the solar concentrator which includes thermal losses, optical losses and direct solar radiation, this balance allows us to calculate the useful power delivered by the receiver which is given by the following formula :

$$Q_u = Q_{ab} - Q_l \quad (1)$$

The power lost is given by the following expression:

$$Q_l = U_l S_{ab} (T_f - T_a) \quad (2)$$

The absorbed solar power is as follows [6]:

$$Q_{abs} = S_c I_d IAM \eta_{opt} K_{ex} K_o \quad (3)$$

With : I_d direct radiation given by the following formula [7]:

$$I_d = DNI * \cos(\Phi) \quad (4)$$

The final power produced is given by the following formula:

$$P_f = Q_u \eta_{th} \quad (5)$$

η_{th} : the thermal efficiency given by the following relation [8]:

$$\eta_{th} = Q_f / Q_a \quad (6)$$

With; Q_f , Q_a useful power delivered by the heat transfer fluid, power absorbed by the receiver.

The factor capacity is given by the following formula:

$$CF = \frac{P_e}{P_n} \quad (8)$$

3. Results and discussion

Using SAM (System Advisor Model) software, we simulated and determined the different characteristics of the Fresnel collector solar power plant, the meteorological data of all sites are sorted from the NREL (National Renewable Energy Laboratory) database. The Figure 3 shows the annual average wind speed at three sites (Tamanrasset, Laghouat and Mascara). It can be seen that the wind speed is not really violent on the different sites during the whole year, the maximum value is 5.45 m.s^{-1} in Laghouat.

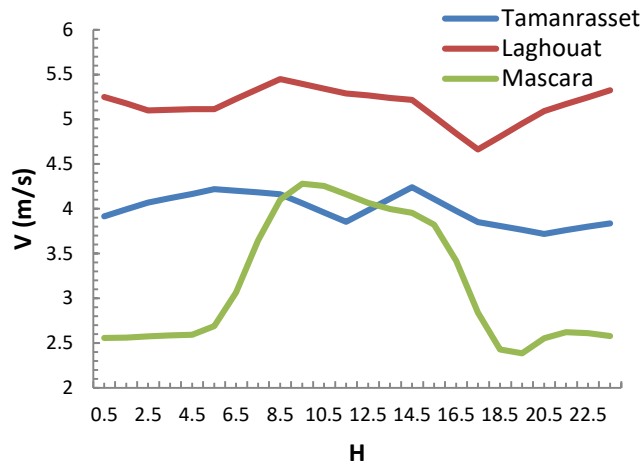


Figure 3. Annual average wind speed ($\text{m}\cdot\text{s}^{-1}$).

The Figure 4 illustrates an analysis of the normal direct sunshine (DNI), we see that the curve is in the shape of a well-symmetrical bell, the region of Tamanrasset receives the maximum annual average value of direct sunshine reaches $803.9 \text{ W}\cdot\text{m}^{-2}$.

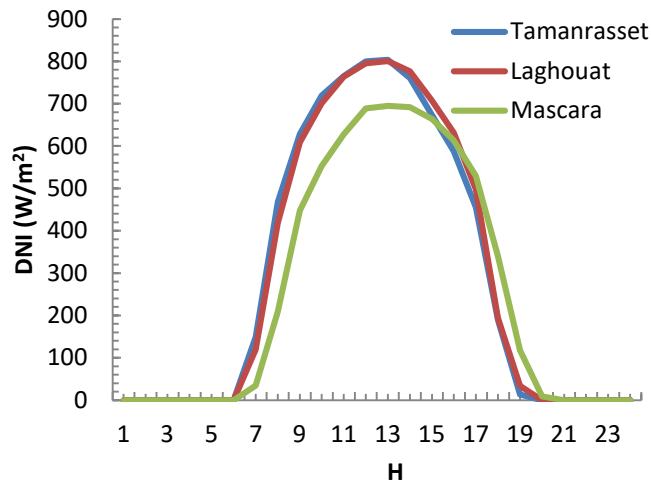


Figure 4. Average annual DNI ($\text{W}\cdot\text{m}^{-2}$).

The Figure 5 shows the evolution of the yield of the solar power plant as a function of the solar multiple (SM) in the site of Tamanrasset, we see that the increase of the SM leads to the increase of the CF, we also see

that when $SM = 4$ the yield of the plant is equal to 47.7 % beyond this value the yield increases slightly almost stable. The Figure 6 shows the annual energy delivered on an hourly scale, it is clear that the maximum annual energy delivered from the plant is about $3,38 \cdot 10^8$ KWh obtained in the site of Tamanrasset, $3,32 \cdot 10^8$ KWh in Laghouat and $2,83 \cdot 10^8$ KWh in Mascara.

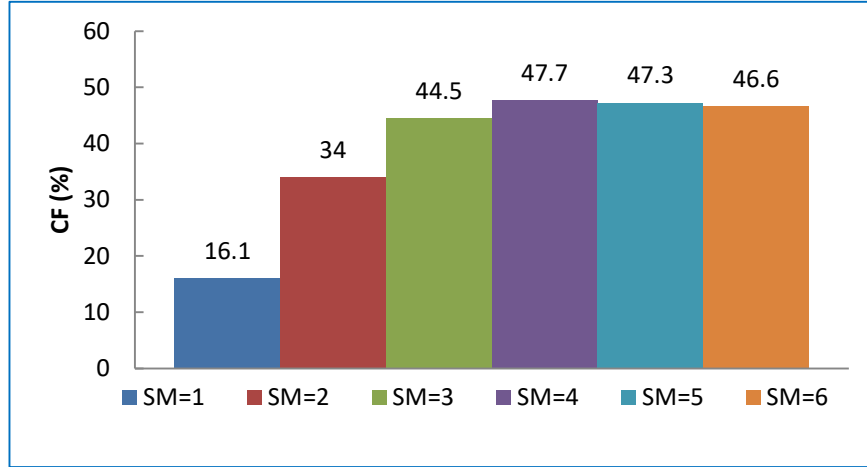


Figure 5. Capacity factor as a function of Solar Multiple.

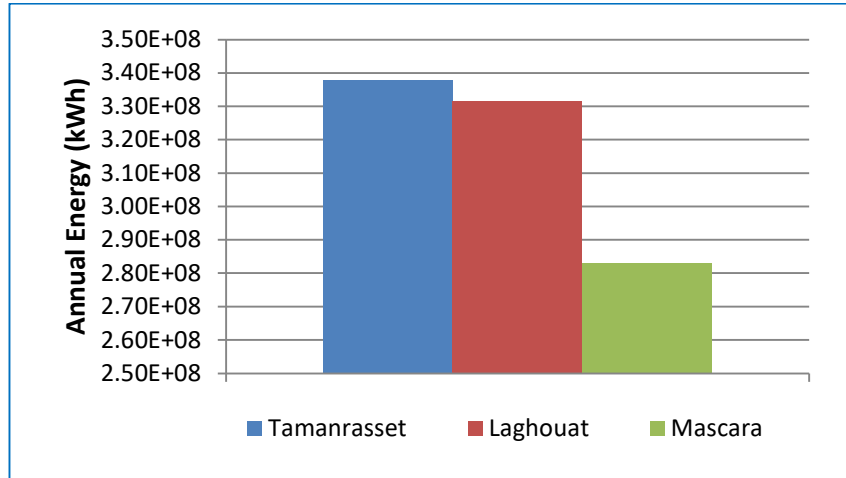


Figure 6. Annual energy delivered in (KWh).

The table below represents the tenico-economic characteristics of the central soil in the regions of Tamanrasset, Laghouat and Mascara.

we have taken into consideration the following parameters; Levelized COE (nominal), Levelized COE (real), Net savings with system (year 1) and Net capital cost. This study allowed us to make a better decision to install this type of Fresnel mirror solar power plants. The results clearly show that the site of Tamanrasset provides a good efficiency and a less LECO.

Table 2. Technical and economic data sheet of the solar power plant in the regions of Tamanrasset, Laghouat and Mascara.

Metric	Tamanrasset	Laghouat	Mascara
Annual energy (year 1)	413 MWh	331 MWh	283 MWh
Capacity factor (year 1)	47.2%	37.8%	32.3%
Annual Water Usage	38,709 m ³	30,245 m ³	26,189 m ³
Levelized COE (nominal)	14.57 ¢/kWh	13.42 ¢/kWh	15.65 ¢/kWh
Levelized COE (real)	11.56 ¢/kWh	10.65 ¢/kWh	12.43 ¢/kWh
Electricity bill without system (year 1)	\$104,412	\$104,412	\$104,412
Net savings with system (year 1)	\$11,306,717	\$-8,929,897	\$7,626,305
Simple payback period	NaN	NaN	NaN
Net capital cost (\$)	773,143,488	546,813,184	546,813,184
Equity (\$)	386,571,744	273,406,592	273,406,592

4. Conclusion

In this study, we examined the effect of wind speed, solar radiation, efficiency and annual energy delivered in different sites in Algeria was presented, The simulation was carried out using the SAM software, we took the weather conditions of Tamanrasset, Laghouat and Mascara. The results obtained in this work have allowed to make the following conclusions:

- ✓ The site of Tamanrasset is the most favorable site with optimal delivered annual energy is 413 MWh.
- ✓ The Direct Normal Irradiation (DNI) for all regions is very encouraging for the installation of Fresnel collector solar plants, the optimal value obtained is 803.9 W.m⁻².
- ✓ The efficiency of the solar power plant increases proportionally with Multiple Solar.

- ✓ It is also concluded that the site of Tamanrasset is more optimal and favorable compared to the other sites examined, the values of Levelized COE (nominal) and Levelized COE (real) are 14.57 ¢\$/kWh and 10.46 ¢\$/kWh, respectively.
- ✓ Wind speed is not a disadvantage at all sites and does not pose a risk for Fresnel mirror solar plants.

References

- [1] C. Voyant, “Prédiction de séries temporelles de rayonnement solaire global et de production d’énergie photovoltaïque à partir de réseaux de neurones artificiels,” vol. 6134, p. 257, (2011).
- [2] I.Tabet., Na.Bellel “Étude , Réalisation et simulation d ’ un capteur solaire,” (2016), [Online]. Available: <https://www.theses-algerie.com/3402521914510541>.
- [3] D. D. E. Presse, “Bilan EDF 2009:[Online]. Available: <https://www.territoire-energie.com/wpcontent/upload> . seen on January 15,(2023).
- [4] Together for more energy, sonelgaz [Online]. Available: <https://www.sonelgaz.dz/fr#overview>. www.sonelgaz.dz.” seen on April, (2023)
- [5] D. E. Benhadji Serradj, A. B. Sebitosi, and S. O. Fadlallah, “Design and performance analysis of a parabolic trough power plant under the climatological conditions of Tamanrasset, Algeria,” *Int. J. Environ. Sci. Technol.*, vol. (2021).
- [6] J. A. D. Deceased and W. A. Beckman, *Solar engineering of thermal processes*, vol. 3, no. 3. (1982).
- [7] A. M. Patnode, S. A. Klein, and D. T. Reindl, “Simulation and performance evaluation of parabolic trough solar power systems,” *Am. Sol. Energy Soc. - Sol. 2006 35th ASES Annu. Conf., 31st ASES Natl. Passiv. Sol. Conf., 1st ASES Policy Mark. Conf., ASME Sol. Energy Div. Int. Sol. Energy Conf.*, vol. 1, pp. 176–181, (2006).
- [8] O. García-Valladares and N. Velázquez, “Numerical simulation of parabolic trough solar collector: Improvement using counter flow concentric circular heat exchangers,” *Int. J. Heat Mass Transf.*, vol. 52, no. 3–4, pp. 597–609, (2009).



Optimal design of solar energy-based hydrogen refueling station: a case study of Touggourt, Algeria

Ahmed Zouhir Kouache^{1*}, Ahmed Djafour¹, Khaled Mohammed Said Benzaoui¹, Souheil Touili¹ and Madjida Ramdani¹

¹ *Faculté des Sciences Appliquées, Laboratoire LAGE, Univ Ouargla, Ouargla 30 000, ALGERIE.*

* *Corresponding author: Tel +213656255992; E-mail: kouache.ahmed@univ-ouargla.dz
DOI: <https://doi.org/10.58452/jpcr.v2i2.158>*

Article history

Received April 24, 2023

Accepted for publication November 02, 2023

Abstract

Carbon production is growing globally, with energy-related carbon emissions accounting for two-thirds of global emissions. Generating carbon-neutral hydrogen from renewable energy is a significant achievement toward a circular economy in this industry. Hydrogen can contribute to reducing gas emissions in the future decades, not just as a potential technology for the future but as a successful technology already being implemented globally. Hydrogen is required for the clean transportation sector and multiple different industrial applications. However, the high cost of clean hydrogen production reduces the rapid development of renewable energy projects established on hydrogen production. So, optimizing design is required to choose the optimum solutions for clean hydrogen production. In this context, this short paper aims to investigate a techno-economic optimization of a hydrogen refueling station with a 262 kg/day capacity in Touggourt City, Algeria (latitude of 33° 6.3' N and the longitude of 6° 4.0' E), based on photovoltaic energy resources. The paper analyses the configuration of a

stand-alone PV system with batteries. The analysis of this arrangement is based on the solar potential at the site, costs of various equipment, electrical load, and hydrogen load. Thus, the study aims to identify the optimized capacity of PV arrays, electrolyzers, batteries, power converters, and hydrogen tanks.

Keywords: Solar energy, Green hydrogen, Hydrogen refueling station, Optimal sizing, Techno-economic, Touggourt region.

1. Introduction

The World's energy need is escalating drastically, and energy production is primarily dominated by oil and coal-based energy generation systems. Fossil fuels are available in limited amounts and cause greenhouse emissions[1]. Moreover, the transportation sector consumes a considerable amount of total fossil fuel and generates vast quantities of carbon dioxide. In the last decades, there has been an increasing need for renewable energy production to reduce greenhouse gas emissions and improve the sustainability of cities[2]. Particularly in the transport industry, using electric, hybrid, and fuel cell vehicles permits considerably reduces gas emissions [3].

Furthermore, population growth has caused several countries to focus on renewable energies that are less expensive and sustainable to meet their electrical demands [4]. To address these challenges, producing electrical energy utilizing photovoltaic systems is being employed to convert solar to electrical energy using PV systems and solar concentrators, which have been effective in several countries [5]. Other familiar sources of renewable energy that prove high potential include geothermal, tidal energy, and wind power [6]. The applications of renewable energy in different sectors have been reported, among which electric and green hydrogen vehicles lead to future transportation [7]. Green hydrogen (GH_2) is a superb fuel with a high-power storage capacity, and its combustion generates only water without causing ecological pollution. Moreover, H_2 has a cost-effective advantage over batteries storages because it can stock energy for long-term periods [8].

On another note, in recent years, much work has been done on modeling and evaluating renewable energy systems to facilitate their deployment and analyze their behavior and performance in different scenarios. For the modeling and simulation of hybrid systems, several software tools, including HOMER, TRNSYS, RETScreen, and Dymola/Modelica, have been created [9]. Hybrid Optimization of Multiple Energy Resources (HOMER) software[10] is one of the software that has found applications in numerous energy feasibility and optimization analyses. The software

*Special Issue of the National Seminar of physics, Chemistry and their Applications "NSPCA '23"
March 6-7th, 2023, Mohamed El Bachir El Ibrahimi University, Bordj-Bou-Arreidj, Algeria.*

has been utilized to conduct feasibility studies of various energy systems, each indicating positive outcomes. Therefore, this paper provides an optimal design and techno-economic analysis of a hydrogen refueling station based on a photovoltaic power system in Touggourt (Algeria). HOMER Pro software was used to design and optimize the renewable power system. The photovoltaic array was utilized as a critical power source to feed the electric load requirement and supply the electrolyzer for hydrogen production. During the surplus times, additional electrical energy was utilized to recharge the battery series.

2. Location of the study

Touggourt is located in the southeast of Algeria at the latitude of $33^{\circ} 6.3'$ N and the longitude of $6^{\circ} 4.0'$ E and is considered in this study as shown in Fig. 1. The city is approximately 660 km away from the capital city of Algeria. The Touggourt community has significantly high global radiation throughout the year.



Figure 1. The geographical location of Touggourt.

3. The load profile

The load assessment of the refueling station (RFS) presented in this section has a daily average load of 13.53 kWh/day for the electric load, whereas the hydrogen load with 262 kg/day.

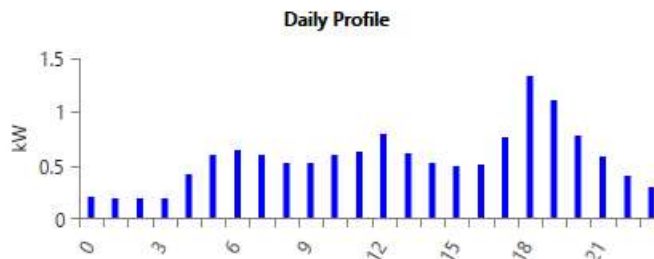


Figure 2. Hourly average electric load variations.

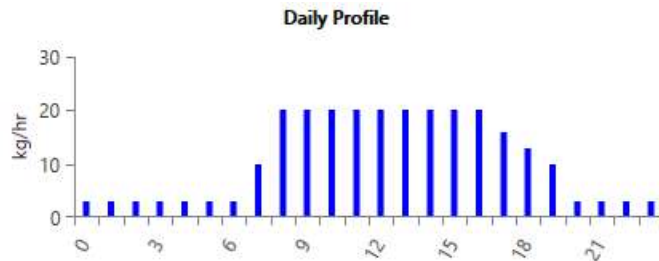


Figure3. Hourly average hydrogen load variations.

As shown in Fig. 3 and 4, the hourly average daily load variations for both the electrical and hydrogen. It is noted that the daily peak electric load occurs at 18 h, where the highest value of hydrogen load was recorded at 8 h to 16 h with 20kg.

4. System Configuration

The proposed system consists of photovoltaic cells, batteries, and an electrolyzer to store hydrogen in a hydrogen tank and a converter. HOMER Pro software was used to model the system to meet the energy needs of the hydrogen refueling station. Fig. 2 shows the schematic of the stand-alone system.

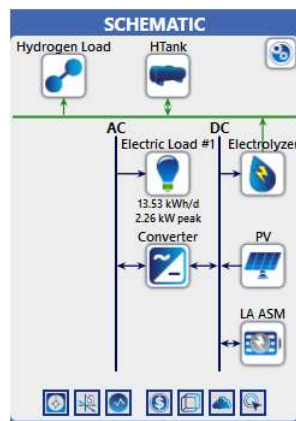


Figure4. Schematic of the proposed system.

The energy management in the system is carried out as follows: the PV feeds the desired load demand and powers the electrolyzer to generate H_2 and stored in the hydrogen tank for refueling station, and charging batteries if the battery's SOC is minimum until the total capacity of the battery is reached, the batteries are required to provide electricity to loads during nights.

5. Optimization results

After the simulation process with Homer software and considering the capacities of different system components, the capacities are obtained and presented in Table 1 presents the optimum configurations. The 100% renewable energy system would have a PV capacity of 28.056 MW, an electrolyzer power capacity of 1.2 MW, a hydrogen tank of 17000 kg, a 2.424 MW power converter, and 2.06 kWh of batteries.

Table 1. Optimized system component sizing.

Component	Size
Generic kWh Lead Acid [ASM]	two batteries of 1.03 kWh
Generic Electrolyzer	1200 Kw
Generic flat plate PV	28056 Kw
Hydrogen Tank	17000 kg
System Converter	2.424 Kw

The PV system produces around 52 077,940 kWh per year of electricity with a maximum power of 28 056 kW produced at noon, as shown in Fig. 5. The generated electricity decreases continuously to reach zero at 6.00 pm.

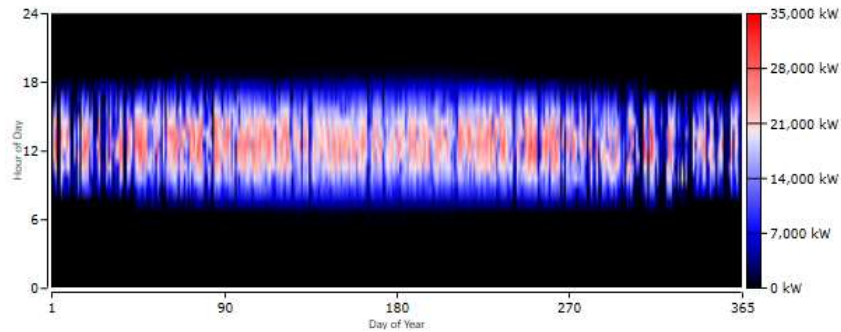


Figure5. PV Power Output.

The electrolyzers consume electricity to produce hydrogen from water. To minimize the cost of green hydrogen production, the electrolyzers are turned on during sunny hours, as shown in Fig. 6, as at this time, the electricity produced by PV panels is available. The electrolyzers are turned off from 6.00 pm to 8.00 am as the PV system provides no green electricity.

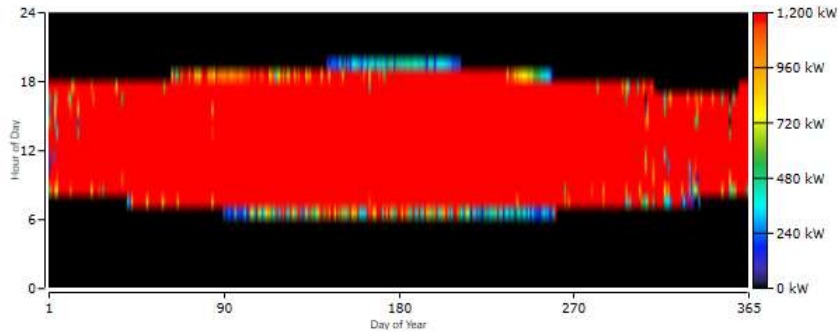


Figure6. Electrolyzer input power.

The monthly hydrogen produced in the electrolyzer is shown in Fig. 7. There is a close agreement between the electricity generated by the PV and the hydrogen produced by the electrolyzer; the amount of hydrogen produced is related to the supplied electricity since electricity is used to initiate the electrochemical process observed during water electrolysis.



Figure 7. The monthly hydrogen produced

The performance of the battery system during the charging and discharging cycles is presented in Fig. 8, where the batteries' daily and hourly State Of Charge is plotted. We noticed that the battery system has the lowest SOC during the autumn and winter.

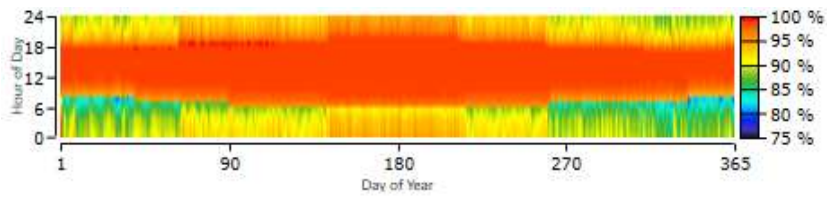


Figure8.State Of Charge.

The hydrogen produced by electrolyzers is stored in special tanks for the refueling station. The hydrogen tank level variation versus the day of the year for a whole year is given in Fig. 9.

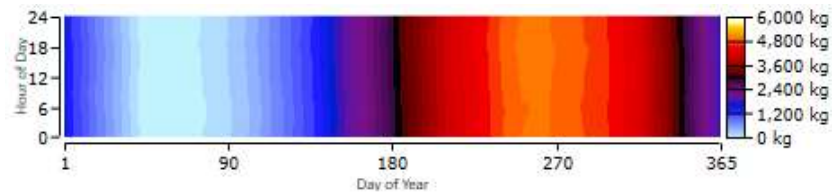


Figure9. Tank Level.

6. Cost optimization

In the price optimization technique, HOMER Pro simulates every system design and shows the possible ones, organized by the Net Present Cost. As defined in Eq (1), the cost of the system (C_S) is the total price of its elements (the cost of the PV system (C_{PV}), the cost of the PEM electrolyzer (C_{Elect}), the cost of the H_2 tank (C_{H_2T}), the cost of batteries (C_B) and the converter cost (C_C)).

$$C_S = C_{PV} + C_{Elect} + C_{H_2T} + C_B + C_C \quad (1)$$

The following formula gives the cost of every part:

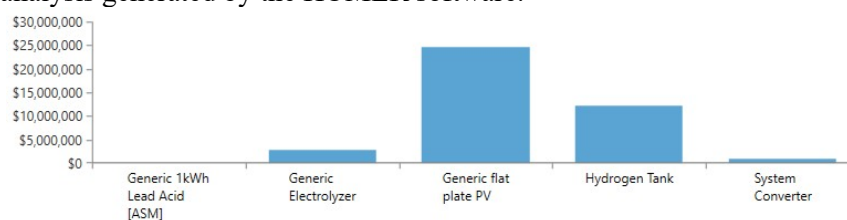
$$C_i = N_i [C_{Cap,i} + (C_{Rep,i} + N_{r_i}) + C_{OM,i}] \quad (2)$$

where N_i : is the number of the element of the HES, $C_{Cap,i}$: is the capital cost of each component, $C_{Rep,i}$: is the replacement cost of each component, N_{r_i} : number of replacements suffered, $C_{OM,i}$: the operation and maintenance price of each component [11]. Tab. 2 summarizes the related costs of each system component; the overall COE rate was \$638.03.

Table 2. The cost of the system and its components.

Component	Capital (\$)	Replacement (\$)	O&M (\$)	Salvage (\$)	Total (\$)
Generic 1kWh Lead Acid [ASM]	14,400.00	5,532.35	6,205.21	1,746.32	24,391.24
Generic Electrolyzer	2,400,000.00	0.00	465,390.60	0.00	2,865,390.60
Generic flat plate PV	19,639,185.66	0.00	5,077,717.95	0.00	24,716,903.61
Hydrogen Tank	11,050,000.00	0.00	1,098,838.91	0.00	12,148,838.91
System Converter	727,124.02	308,499.69	0.00	58,062.76	977,560.95
System	33,830,709.67	314,032.04	6,648,152.66	59,809.07	40,733,085.31

Fig. 10 displays the Cost summary of all the components considered in the analysis generated by the HOMER software.

**Figure 10.** Cost summary.

As displayed in Fig. 10, it can be seen that the PV has the highest total cost of \$ 24,716,903.61, whereas the battery has the least total cost of \$ 24,391.24.

7. Conclusion

This work offered an optimal design of a stand-alone photovoltaic system with battery storage. This configuration fed a hydrogen refueling station of 13.53 kWh/day electric and 262 kg/day hydrogen in Touggourt city. HOMER Pro was utilized to optimize the behavior of the power system. The results were compared to identify the better size of the system based on the least overall Net Present Cost and Cost of Energy. The optimum finding outcomes presented a 28056 kW PV array, two batteries of 1.03 kWh each, a 2.424 kW converter, a 1200 kW electrolyzer, and a 17000 kg hydrogen reservoir was the best choice to equip the hydrogen refueling station. Future work includes adding other renewable energy sources to make a hybrid system for hydrogen refueling stations to minimize the capacity of the PV modules.

References

- [1] P. Malik, M. Awasthi, and S. Sinha, "A techno-economic investigation of grid integrated hybrid renewable energy systems," *Sustainable Energy Technologies and Assessments*, vol. 51, p. 101976, 2022/06/01/ 2022. <https://doi.org/10.1016/j.seta.2022.101976>.
- [2] E. M. Barhoumi, P. C. Okonkwo, I. Ben Belgacem, M. Zghaibeh, and I. Tlili, "Optimal sizing of photovoltaic systems based green hydrogen refueling stations case study Oman," *International Journal of Hydrogen Energy*, vol. 47, no. 75, pp. 31964-31973, 2022/09/01/ 2022. <https://doi.org/10.1016/j.ijhydene.2022.07.140>.
- [3] A. Ajanovic and R. Haas, "Prospects and impediments for hydrogen and fuel cell vehicles in the transport sector," *International Journal of Hydrogen Energy*, vol. 46, no. 16, pp. 10049-10058, 2021/03/03/ 2021. <https://doi.org/10.1016/j.ijhydene.2020.03.122>.
- [4] I. Yuksel and K. Kaygusuz, "Renewable energy sources for clean and sustainable energy policies in Turkey," *Renewable and Sustainable Energy Reviews*, vol. 15, no. 8, pp. 4132-4144, 2011/10/01/ 2011. <https://doi.org/10.1016/j.rser.2011.07.007>.
- [5] A. S. Al Busaidi, H. A. Kazem, A. H. Al-Badi, and M. Farooq Khan, "A review of optimum sizing of hybrid PV–Wind renewable energy systems in oman," *Renewable and Sustainable Energy Reviews*, vol. 53, pp. 185-193, 2016/01/01/ 2016. <https://doi.org/10.1016/j.rser.2015.08.039>.
- [6] E. M. Barhoumi, S. Farhani, P. C. Okonkwo, M. Zghaibeh, and F. Bacha, "Techno-economic sizing of renewable energy power system case study Dhofar Region-Oman," *International Journal of Green Energy*, vol. 18, no. 8, pp. 856-865, 2021/06/21 2021. 10.1080/15435075.2021.1881899.
- [7] J. Van Mierlo, G. Maggetto, and P. Lataire, "Which energy source for road transport in the future? A comparison of battery, hybrid and fuel cell vehicles," *Energy Conversion and Management*, vol. 47, no. 17, pp. 2748-2760, 2006/10/01/ 2006. <https://doi.org/10.1016/j.enconman.2006.02.004>.
- [8] J. d. I. Cruz-Soto, I. Azkona-Bedia, N. Velazquez-Limon, and T. Romero-Castanon, "A techno-economic study for a hydrogen storage system in a microgrid located in baja California, Mexico. Levelized cost of energy for power to gas to power scenarios," *Int. J. Hydrog. Energy*, 2022/04/02/ 2022. <https://doi.org/10.1016/j.ijhydene.2022.03.026>.
- [9] S. Boulmrharj, M. Khaidar, M. Bakhouya, R. Ouladsine, M. Siniti, and K. Zine-dine, "Performance Assessment of a Hybrid System with Hydrogen Storage and Fuel Cell for Cogeneration in Buildings," vol. 12, no. 12, p. 4832, 2020.
- [10] *Hybrid Optimization of Multiple Energy Resources (HOMER) software* Available: <https://www.homerenergy.com>
- [11] S. Peláez-Peláez, A. Colmenar-Santos, C. Pérez-Molina, A.-E. Rosales, and E. Rosales-Asensio, "Techno-economic analysis of a heat and power combination system based on hybrid photovoltaic-fuel cell systems using hydrogen as an energy vector," *Energy*, vol. 224, p. 120110, 2021/06/01/ 2021. <https://doi.org/10.1016/j.energy.2021.120110>.



Evolution with temperature of point defects concentration in Fe_2ZrX ($X=\text{V}, \text{Y}, \text{Tc}, \text{Ru}$): DFT and Wagner-Schottky modeling

Lyacine Rabahi^{1,2*}, Leila Rouaiguia² and Abdelhafid Kellou²

¹ Research Center in Industrial Technologies CRTI, P. O. Box 64, Cheraga 16014, Algiers, Algeria.

² Laboratoire de Physique Théorique, Faculté de Physique, USTHB, BP 32 El Alia, 16111, Bab Ezzouar, Alger, Algeria.

* Corresponding author: E-mail address: rabahil@yahoo.fr

DOI : <https://doi.org/10.58452/jpcr.v2i2.160>

Article history

Received April 15, 2023

Accepted for publication December 02, 2023

Abstract

The evolution with temperature of the point defect concentration in the cubic C15- ZrFe_2 Laves phase was investigated in the presence of several ternary additions X ($X=\text{V}, \text{Y}, \text{Tc}, \text{Ru}$). The heats of formation of the different point defects were carried out at 0K by means of DFT calculations. The Wagner-Schottky Model, based on substitutional and interstitial sublattices configuration within the canonical ensemble, was applied to investigate temperature effects on the defect concentration. The main results show a strong dependency of the C15- Fe_2Zr stability on the point defect type. Energetically, the Ru^{Fe} antisite is the most stable defect at low temperatures (0 K), whereas the Va^{Fe} , Va^{Zr} , and Y^{Fe} are the least stable ones. At finite temperatures, it was found that antisites are the dominant constitutional defects on both sides of stoichiometry in the C15- ZrFe_2 compound.

Keywords: Point Defect, Laves Phases, DFT, Wagner-Schottky Model.

Introduction

Laves phases with topologically close-packed structures, are very attractive materials for high temperature structural applications [1]. They are also considered as superconducting materials and giant

Special Issue of the National Seminar of physics, Chemistry and their Applications "NSPCA '23" March 6-7th, 2023, Mohamed El Bachir El Ibrahimi University, Bordj-Bou-Arreidj, Algeria.

magnetostrictive materials, owing to their excellent physical and chemical properties [2]. However, the off-stoichiometry, that concerns about 25% of Laves phases, affects strongly the physical, mechanical and functional properties of these materials and therefore has a decisive impact on their performance in application [3,4]. In this context, vacancies and antisite defects, which are the main reasons of off-stoichiometry, assist the movement of Synchro-Shockly dislocations, thus facilitating the synchroshear deformation mechanism and modify the mechanical properties of Laves phases [2,5]. Moreover, vacancies play important role in diffusion of doping atoms and atomic self-diffusion in solid materials. In that way, point defects become an important topic in materials science that must be carefully investigated.

To date, several experimental and theoretical works have been done to study the point defects in Laves phases. Experimentally, antisites are found to be responsible for the off-stoichiometry observed in Fe_2Nb , Cr_2Nb and Co_2Nb compounds [5,6]. Whereas applying first-principles calculations, together with a statistical models, it was found that antisite defects are favored than vacancies on both sides of stoichiometry for Mg_2Ca and Zn_2Mg with C14 structure [3,4]. In addition, Zn2 vacancies are also favorable under moderate Mg-rich condition in Zn_2Mg Laves phases [4]. Another theoretical study, found that Mn antisites are the most favorable defects broadening the homogeneity range of the Mn_2Zr phase toward the Mn-rich side [7]. With C15 Laves structure, similar behaviors of point defects are evidenced. Namely, antisite defects on both sides of off-stoichiometry in the Cu_2Mg Laves phase [2], Co_2Zr , Cr_2Nb [8], Co_2Zr [1] as well as several Cr-based Laves phases [9]. The effects of alloying elements are also investigated in some studies [2,8], nevertheless, the mechanisms of point defects formation and alloying elements effects on the overall trend of the point defects at lower and high temperatures are still poorly understood. In view of this, the present work aims at giving new insights on how finite temperature and alloying elements affect the intrinsic point defect behavior in the C15- Fe_2ZrX system, with X being V, Y, Tc and Ru. Our choice of elements is motivated by the interesting results obtained by rabahi et al [10]. The relative stability of point defects in the C15- Fe_2Zr compound is determined from the calculated formation enthalpies of point defects, obtained in the framework of DFT calculations. The statistical Wagner-Schottky model is applied to investigate effect of both temperature and X alloying elements on the point defects behavior in the C15- ZrFe_2X Laves phase. The present paper is

organized as follows. The technical details of the DFT calculations and the Wagner-Schottky model are presented in Sec. 2. The main results are discussed in Sec. 3. While concluding remarks are given in Sec. 4.

2. Computational Details

2.1 DFT calculations

The present study calculations were performed basing on the density functional theory (DFT) using pseudopotential method as implemented in the Quantum-Espresso [11]. The many-body problem of interacting electrons and nuclei was treated using a series of one-electron equations, the so-called Kohn-Sham (KS) equations [12,13]. The generalized gradient approximation (GGA) of Perdew et al (PBE) to the local density approximation, was taken to include the exchange-correlation energy [14] and ultrasoft pseudopotentials of Vanderbilt were used [15]. A kinetic energy cut-off of 40 Ry and a well converged value of the k-point mesh over the Brillouin zone were considered, Namely, 6 6 6 for the C15 supercell. All structures were allowed to fully relax using Broyden- Fletcher-Goldforb-Shanno (BFGS) scheme [16] until the total energy has converged to less than 10^5 eV/atom. The maximum force has converged to lower than 0.004 eV/Å.

2.2 Wagner-Schottky model

Deviations from the ideal stoichiometric compositions are always accommodated by the creation of constitutional point defects (e.g. vacancies, antisites, ternary substitutional or interstitial atoms) on one or both sublattices. Thermal defects are also activated at finite temperature in addition to the constitutional ones, in order to maintain the overall composition of the alloy. To allow the use of the Wagner-Schottky model, two assumptions must be considered. (i) The defect concentrations are sufficiently dilute i.e gaz of non-interacting (isolated) atoms and point defects. (ii) At constant pressure, the internal energy, volume, and vibrational entropy of the crystal are linear functions of the number of atoms or vacancies in the different sublattices. We consider a canonical ensemble containing a fixed number of atoms, N_{at} , and the total number of lattice sites N_s may thus vary when vacancies are present, consequently, it is more convenient to describe the distribution of alloy components between the sublattices in terms of atomic concentrations defined with respect to the total number of atoms N_{at} . The atomic concentration of species i in

sublattice m is defined as:

$$x_i^m = \frac{N_i^m}{N_{at}} \quad (1)$$

Where N_i^m is the number of species i on the sublattice m with $i=\{A, B, Va\}$ and $m=\{\alpha, \beta\}$. The ordered C15-AB₂ structure can be divided into two sublattices: the α sublattice, normally occupied by A atoms, and the β sublattice, normally occupied by B atoms, therefore, the number of A atoms $N_A = N_A^\alpha + N_A^\beta$, and the number of B atoms $N_B = N_B^\alpha + N_B^\beta$ are fixed. The number of vacancies in the alloy N_{Va} as well as the number of lattice sites may vary. In this case, the equilibrium state of the alloy at temperature T and pressure P is determined by the minimization of the Gibbs free energy G, or, equivalently, of its excess value ΔG defined relative to some standard states and normalized per atom.

$$\Delta G = \Delta H - T\Delta S \quad (2)$$

Where ΔH is the enthalpy (or heat) of alloy formation and ΔS is the entropy. According to this model, the formation enthalpy (per atom) of alloy is a linear function of the point defect concentrations.

$$\Delta H = \Delta H_0^f + \sum_d H_d x_d \quad (3)$$

where x_d is the atomic concentration of defects of type d defined as the total number of defects divided by the total number of atoms in the system, with $d=\{\text{vacancies, antisites}\}$. H_d is the formation enthalpy of isolated point defects of type d in stoichiometric structure. ΔH_0^f is the formation enthalpy of the fully ordered stoichiometric alloy. Here, the effects of vibrational entropy are neglected and only the configurational entropy is taken into account.

$$\Delta S = k_B \ln \left(\prod_m \frac{N_s^{m!}}{(\prod_i N_i^{m!})} \right) \quad (4)$$

where k_B is Boltzmann's constant and N_s^m is the total number of sites on the m sublattice. When considering the substitutional atoms, the entropy (per atom) of alloy can be written as:

$$\Delta S = k_B (1 + x_{Va}^{sub}) \left(\frac{2}{3} \ln(2) + \ln \left(\frac{1+x_{Va}^{sub}}{3} \right) \right) - k_B \sum_i \sum_j x_j^i \ln(x_j^i) \quad (5)$$

where $i=\{\alpha, \beta\}$ and $j=\{A, B, X, Va\}$.

The equilibrium concentrations of point defects can now be obtained through a minimization of the Gibbs free energy of the system ΔG , which together with mass-balance constraints leads to the following

set of non-linear equations:

$$\frac{3 x_A^\beta x_{Va}^\alpha}{x_{Va}^\beta (2 - 3x_B^\alpha - 3x_X^\alpha + 2x_{Va}^\beta - x_{Va}^\alpha)} = \exp \left[-\frac{H_A^\beta + H_{Va}^\alpha - H_{Va}^\beta}{k_B T} \right] \quad (6a)$$

$$\frac{3 x_B^\alpha x_{Va}^\beta}{x_{Va}^\alpha (1 - 3x_A^\beta - 3x_X^\beta - 2x_{Va}^\beta + x_{Va}^\alpha)} = \exp \left[-\frac{H_B^\alpha + H_{Va}^\beta - H_{Va}^\alpha}{k_B T} \right] \quad (6b)$$

$$\frac{x_X^\beta x_{Va}^\alpha}{x_{Va}^\beta x_X^\alpha} = \exp \left[-\frac{H_X^\beta - H_X^\alpha - H_{Va}^\beta + H_{Va}^\alpha}{k_B T} \right] \quad (6c)$$

$$\frac{27 x_{Va}^\beta (x_{Va}^\alpha)^2}{4 (1 + x_{Va}^\beta + x_{Va}^\alpha)^3} = \exp \left[-\frac{H_{Va}^\beta + 2H_{Va}^\alpha}{k_B T} \right] \quad (6d)$$

$$x_A = x_A^\beta + \frac{1}{3} (2 + 2x_{Va}^\beta - 3x_B^\alpha - 3x_X^\alpha - x_{Va}^\alpha) \quad (6e)$$

$$x_X = x_X^\alpha + x_X^\beta \quad (6f)$$

At any given total alloy composition and temperature, a numerical solution of Eqs. (6) can give us the equilibrium concentrations of point defects.

3. Results and Discussion

3.1 Point defects in C15 Fe₂ZrX at 0K

In ref [17], the stability and magnetic properties of the clean Fe₂Zr Laves phase were investigated. At the stoichiometric composition, Rabahi et al [17], found that this material is more stable in the C15 Laves structure with the ferromagnetic state. However, presents an extended homogeneity range, between about 34 and 27-28 at % [18] which is always attributed to the point defects creation. Consequently, the first part of this work is devoted to the energetic and behavior of the point defects in C15-Fe₂Zr Laves phase. To this purpose, several compositions were considered for the defected materials, including one of the following six defects: Fe vacancy, Zr Vacancy, Fe antisite, Zr antisite, ternary X substitutional atom for Fe or Zr. Since Laves phases present topologically close packed structure, there are no interstitial sites with a size comparable to that of the component atoms, therefore interstitial defects were excluded. For each composition, the Heats of formation, volume variations and total magnetization were predicted and the results are given in the Table 1. As it can be seen, the stability of the C15-Fe₂Zr compound is affected by the point defects creation, remarkably, Ru^{Fe} defect

increases the stability of the system, while opposite effect is found when vacancies Va^{Fe} , Va^{Zr} and Y^{Fe} antisite are created. Comparatively, the remaining defects slightly destabilize the C15-Fe₂Zr material.

The magnetic properties and total volume are also found to be affected by point defects creation. Fe and Zr vacancies, as well as Zr antisite reduce the unit cell volume, while the Fe antisite induces the opposite effect. For the substitutional X elements, it is found that Ru, V, and Tc increase the volume only when they replace Fe, whereas the case of Y is rather singular, a volume expansion is noticed whatever the nature of the site replaced by Y, these results are explained by size effects as already discussed in ref [10], in addition, the total magnetization obtained for the different configurations is slightly affected and fluctuating around $1.6 \mu_B / Fe$ atom, which is related to the magneto-volume effects.

In the Table 2, the heats of formation of punctual defects predicted at 0 K in the C15-Fe₂ZrX compound are reported. At this temperature, the punctual defects are only governed by their formation enthalpies and the stable ones, are considered as constitutional defects. The deviation toward Zr-rich Fe₂Zr side could be caused either by Zr antisites and/or Fe vacancies. Similarly, the deviation toward Fe-rich Fe₂Zr could be accommodated either by Fe antisites or Zr vacancies. From Table 2, it can be seen that $H_{VaZr} > H_{FeZr}$ and $H_{VaFe} > H_{ZrFe}$. Therefore, it could be concluded that antisites are the dominant constitutional defects in both side of stoichiometry in C15-ZrFe₂ compound. Moreover, all the formation enthalpies values are positives except the anti-site Ru^{Fe}. This means that the creation of defects in the compound C15-Fe₂ZrX is an endothermic reaction which requires a supply of external energy. The Table 2 shows that Fe and Zr vacancies as well as Y^{Fe}, Tc^{Zr}, and Zr^{Fe} anti-sites are the least favorable. While Ru^{Fe}, Tc^{Fe} and V^{Fe} anti-sites are the most favorable. In addition, the Ru and Tc atoms mark a strong preference to Fe site. While, the Y atom prefers the Zr site. The Vanadium V element slightly prefers the Fe site. This behavior of X elements is attributed to the size and electronic effects as already discussed in the work of L. Rabahi et al [10].

3.2 Point defects in C15 Fe₂ZrX at finite temperature

Using the heats of formation values given in the Table 2, the equilibrium point defects are obtained by solving the set of equations 6(a-f) at a given temperature and alloy composition. It is well known that the Wagner-Schottky model, applied in this work is only valid at intermediate and high temperatures. For this reason, several temperatures are considered as a first step, and convergence is reached

from 1373 K (for the Fe_2Zr system) and 1673 K (for the Fe_2ZrX system). Consequently, three temperatures were considered, namely 1373, 1673 and 2073 K, in order to include both temperature and alloy composition effects on the point defects behavior in the C15 Fe_2Zr and C15 Fe_2ZrX systems. As it can be seen (from Figure 1), the point defect structure in the off-stoichiometric Fe_2Zr is very complex, and the concentrations exhibit a brutal change when the alloy composition vary from Zr-rich to Fe-rich side. This fact reflects the strong correspondence between the point defect and its local chemical environment. The Fe and Zr anti-site are found to be the dominant defects in C15- ZrFe_2 even at high temperatures, while the vacancies, and more particularly, Va^{Fe} are the less activated ones, and the less affected by Zr concentration, meaning that, deviation from ideal stoichiometry in the C15- ZrFe_2 is only governed by Fe and Zr anti-sites. This result is similar to the general tendency of point defects in C15 Laves phases found in previous studies [1,2,5,7,8], and could be easily explained by geometrical rules. The smallest Fe atom is apt to replaces larger Zr atom to form anti-site defect on the Zr sublattice [5], however, it is rare for large atom to replace small atom to form the anti-site defect in small atom sublattice. So, according to previous studies, the formation of this kind of defects is feasible in Laves phases with atomic size ratio smaller than the ideal ratio 1.225 [18]. Thus the formation of anti-site defect Zr^{Fe} is possible in the C15- Fe_2Zr , since the atomic sizes of the Fe and Zr atoms are respectively 1.60 \AA and 1.39 \AA , and the atomic size ratio is about 1.15, less than the ideal atomic radii ratio in Laves phases. Moreover, comparing the results obtained at different temperatures, it is found that all the defect concentrations are found to be increased with temperature. This fact is attributed to the thermal defects which are activated in balanced combinations in order to maintain the overall composition of the alloy [8]. The site preference of ternary elements at finite temperature is also investigated in the present work. For each X element, Tc, Ru, V and Y, the corresponding equilibrium point defect concentrations, are obtained and shown in the Figure 2 (a-d) respectively. At $T = 0\text{K}$, rabahi et al [10] found that Y, and Tc elements prefer to substitute for Zr atoms while the Ru and V prefer to replace Fe ones. At finite temperatures, entropy will play an important role in determining the site preference of ternary elements. As shown in Figure 1, all the Ru atoms have substituted to the Fe ones at elevated temperature, in the entire range of Zr composition; this fact is related to the negative heat of formation obtained in the case of the Ru^{Fe} defect. The Tc and Y elements exhibit a strong preference to the Fe and Zr sites

respectively, while moderate preference to the Fe site is noticed for the V element. Finally, the defect concentration curves underwent a noticeable shift towards lower values of Zr concentration in the case of Fe₂ZrY alloy. This fact is due to the sharp variation of the Zr concentration in the system, since a great part of this element is found to be replaced by Y atoms. This last one displays a great preference for the Zr sites, as is clearly visible from the high concentration of the Y^{Zr} defect.

Table 1: Heats of formation, volume variations and total magnetization of Clean Fe₂Zr, defected Fe₂Zr and Fe₂ZrX with C15 Laves phase.

	ΔH_f (eV/atome)	ΔV (%)	M (μ_B /Atome Fe)
Fe ₂ Zr	-0.280	-	1.68
Va ^{Fe}	-0.165	-1.304	1.54
Va ^{Zr}	-0.157	-3.055	1.58
Fe ^{Zr}	-0.247	-1.850	1.83
Zr ^{Fe}	-0.228	3.125	1.60
Ru ^{Fe}	-0.301	1.095	1.75
Ru ^{Zr}	-0.263	-1.450	1.90
V ^{Fe}	-0.267	0.453	1.58
V ^{Zr}	-0.243	-1.705	1.61
Tc ^{Fe}	-0.278	0.719	1.72
Tc ^{Zr}	-0.198	-2.648	1.74
Y ^{Fe}	-0.167	4.314	1.61
Y ^{Zr}	-0.251	1.211	1.68

Table 2: Heats of formation of isolated punctual defects (H_d) predicted at 0 K in the C15-Fe₂Zr compound.

	Va	Fe	Zr	Ru	Y	Tc	V
Fe	2.640	-	1.195	-0.497	2.706	0.037	0.313
Zr	2.822	0.752	-	0.411	0.703	1.975	0.879

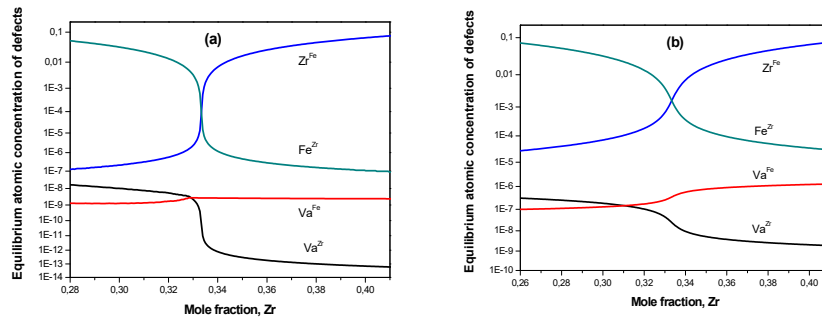


Figure 1: Equilibrium point defect concentrations in C15-Fe₂Zr system at (a) T= 1373 and (b) T= 2073 K as function of Zr concentration.

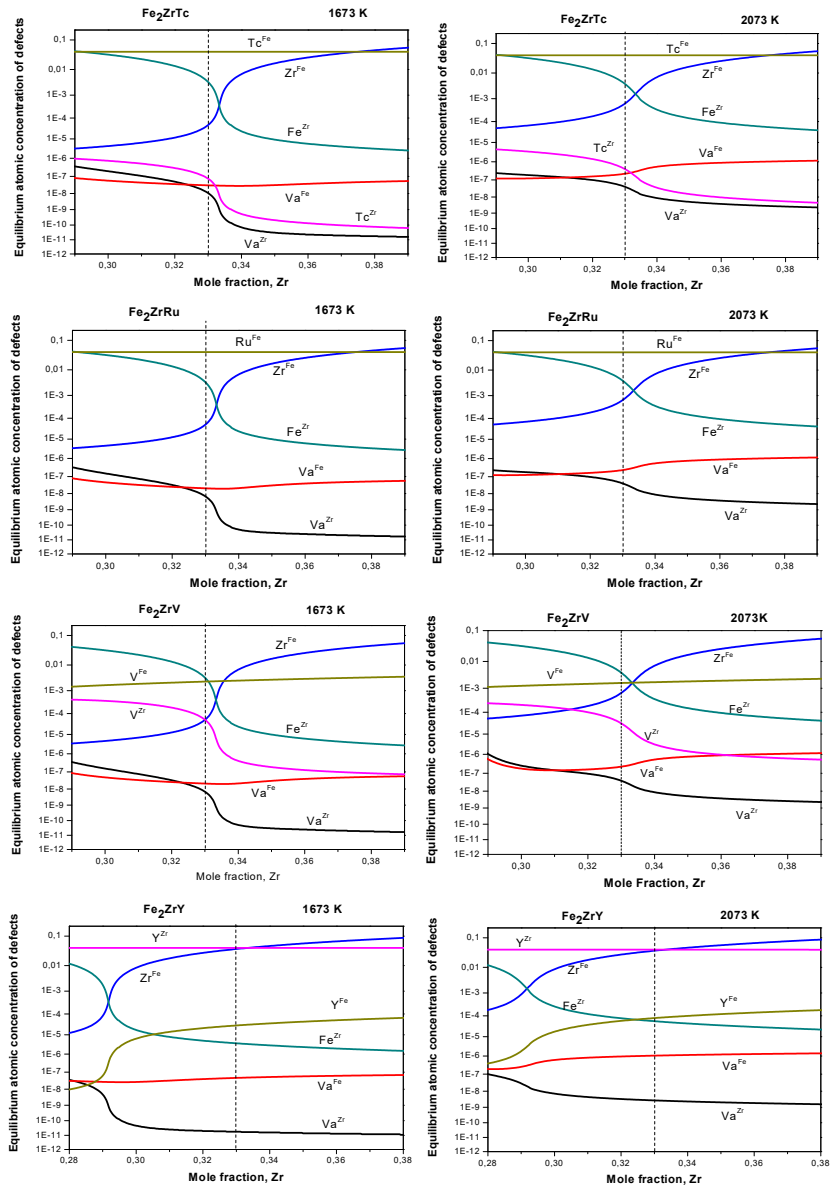


Figure 2: Equilibrium point defect concentrations in C15-Fe₂ZrX, (X =Tc, Ru, V and Y) system at T= 1673 K (left) and T= 2073 K (right) as function of Zr concentration.

4. Concluding remarks

In this work, the evolution with temperature of the point defect concentrations in the C15-ZrFe₂ Laves phase in the presence of several ternary additions X (X=V, Y, Tc, Ru) is investigated. To this purpose, the DFT-based pseudo-potential method combined with the statistical Wagner-Schottky model is applied. The obtained results indicate a strong dependency of the stability of the C15-Fe₂Zr compound on the point defect kind; the RuFe antisite increases the stability of the system, while the opposite effect is found when vacancies VaFe, VaZr and YFe antisite are created. At finite temperature, the antisites are found to be the dominant constitutional point defects, and the entropy plays an important role in determining the site preference of ternary elements. The Ru atoms have substituted for the Fe ones at elevated temperatures and in the entire range of Zr composition, whereas the Tc and Y elements exhibit a strong preference for the Fe and Zr sites, respectively.

References

- [1] C.L. Fu, M. Kremer, First-principles study of point-defect structures in C 15 ZrCo 2 and B 2 ZrCo, Phys. Rev. B. 68 (2003) 1–8. doi:10.1103/PhysRevB.68.134110.
- [2] J. Zheng, X. Tian, L. Shao, X. Pan, P. Tang, B. Tang, Point defects and Zn-doping in defective Laves phase C15 MgCu 2 : A first-principles study, Comput. Mater. Sci. 122 (2016) 159–166. doi:10.1016/j.commatsci.2016.05.026.
- [3] L. Shao, T. Shi, J. Zheng, X. Pan, B. Tang, Intermetallics The native point defects in C14 Mg 2 Ca Laves phase : A first-principles study, 65 (2015) 29–34. doi:10.1016/j.intermet.2015.05.010.
- [4] L. Shao, T. Shi, J. Zheng, H. Wang, X. Pan, B. Tang, First-principles study of point defects in C14 MgZn 2 Laves phase, J. Alloys Compd. 654 (2016) 475–481. doi:10.1016/j.jallcom.2015.09.142.
- [5] J.H. Zhu, L.M. Pike, C.T. Liu, P.K. Liaw, Point defects in binary Laves phase alloys, Acta Mater. 47 (1999) 2003–2018. doi:10.1016/S1359-6454(99)00090-7.
- [6] C.T. Liu, J.H. Zhu, M.P. Brady, C.G. Mckamey, L.M. Pike, Physical metallurgy and mechanical properties of transition-metal Laves phase alloys, 8 (2000) 1119–1129.
- [7] X.Q. Chen, W. Wolf, R. Podloucky, P. Rogl, M. Marsman, Ab initio study of ground-state properties of the Laves-phase compound Zr Mn₂, Phys. Rev. B - Condens. Matter Mater. Phys. 72 (2005) 1–11. doi:10.1103/PhysRevB.72.054440.
- [8] C. JIANG, Site preference of early transition metal elements in C15 NbCr₂, Acta Mater. 55 (2007) 1599–1605.

- doi:10.1016/j.actamat.2006.10.020.
- [9] X.Q. Chen, W. Wolf, R. Podloucky, P. Rogl, Ab initio study of ground-state properties of the Laves phase compounds TiCr₂, ZrCr₂, and HfCr₂, Phys. Rev. B - Condens. Matter Mater. Phys. 71 (2005) 1–11. doi:10.1103/PhysRevB.71.174101.
- [10] L. Rabahi, M. Gallouze, T. Grosdidier, D. Bradai, A. Kellou, ScienceDirect Energetics of atomic hydrogen absorption in C15-Fe 2 Zr Laves phases with ternary additions : A DFT study, Int. J. Hydrogen Energy. (2016) 1–10. doi:10.1016/j.ijhydene.2016.11.131.
- [11] G.B. S. Baroni, A. Dal Corso, S. De Gironcoli, P. Gianozzi, C. Cavazzoni, et al, [Http://www.pwscf.org/](http://www.pwscf.org/). (n.d.).
- [12] W. Hohenberg, P. Kohn, Inhomogeneous Electron Gas., Phys. Rev. 136 (1964) B 864-B 871.
- [13] W. Kohn, L.J. Sham, Self-Consistent Equations Including Exchange and Correlation Effects, Phys. Rev. 140 (1965) A1134–A1138. doi:<http://dx.doi.org/10.1103/PhysRev.140.A1133>.
- [14] J.P. Perdew, K. Burke, M. Ernzerhof, Generalized Gradient Approximation Made Simple, Phys. Rev. Lett. 77 (1996) 3865–3868. doi:10.1103/PhysRevLett.77.3865.
- [15] D. Vanderbilt, Soft self-consistent pseudopotentials in a generalized eigenvalue formalism, Phys. Rev. B. 41 (1990) 7892–7895. doi:10.1103/PhysRevB.41.7892.
- [16] T.H. Fischer, J. Almlof, General methods for geometry and wave function optimization, J. Phys. Chem. 96 (1992) 9768–9774. doi:10.1021/j100203a036.
- [17] L. Rabahi, B. Alili, D. Bradai, T. Grosdidier, A. Kellou, DFT calculations of structural, magnetic and thermal properties of C15, C14 and C36 Laves phases in Fe-Nb-Zr, Intermetallics. 83 (2017) 92–100. doi:10.1016/j.intermet.2016.12.011.
- [18] F. Stein, M. Palm, G. Sauthoff, Structure and stability of Laves phases . Part I . Critical assessment of factors controlling Laves phase stability, 12 (2004) 713–720. doi:10.1016/j.intermet.2004.02.010.



Contribution à l'étude du nettoyage des panneaux photovoltaïques par procédé électrostatique

Zeid Bendaoudi^{1,2*}, Nezha Kadous^{1,3}, Khelifa Yanallah⁴,
Yassine Bellebna² et Amar Tilmatine²

¹ Département d'Electrotechnique et automatique, Université Ahmed Zabana, Relizane, 48000, algérie

² Laboratoire APELEC, Université Djillali Liabes, Sidi Bel-Abbes, 22000, Algérie

³ Département d'Electrotechnique, Université Mustapha Stambouli, Mascara, 20000, Algérie

⁴ Laboratoire LSTE, Université Ibn Khaldoun, Tiaret, 14000, Algérie

* Corresponding author: Tel./Fax: +213-667-136-642;

E-mail: Zeid.bendaoudi@univ-relizane.dz

DOI: <https://doi.org/10.58452/jpcr.v2i2.161>

Historique de l'article

Article reçu March 09, 2023

Accepté pour publication November 02, 2023

Resume

Le but de cette étude est d'examiner l'utilisation d'un vent électrique généré par une décharge couronne à deux électrodes pour nettoyer les panneaux photovoltaïques de la poussière. La première électrode est un fil alimenté par la haute tension continue négative allant jusqu'à 30 kV, tandis que la seconde est reliée à la terre. Le dispositif permet de générer un vent ionique et se déplacer sur toute la surface du panneau en nettoyant la poussière. L'alimentation de l'actionneur de nettoyage à décharge couronne est assurée par la cellule photovoltaïque elle-même, et le nettoyage électrostatique par décharge couronne peut atteindre un taux de nettoyage de 90 % et améliorer l'efficacité des panneaux photovoltaïques. Cette technologie offre l'avantage d'un nettoyage à sec par des phénomènes électrostatiques et à tout moment, avec une faible consommation d'énergie, le courant étant pratiquement nul, de l'ordre des micro-ampères.

Mots Clés : décharge couronne, haute tension, nettoyage, panneaux photovoltaïques.

1. Introduction

Special Issue of the National Seminar of physics, Chemistry and their Applications "NSPCA '23"
March 6-7th, 2023, Mohamed El Bachir El Ibrahimi University, Bordj-Bou-Argeridj, Algeria.

L'énergie solaire photovoltaïque est une source d'énergie renouvelable très prometteuse en raison de son caractère propre et inépuisable. Toutefois, la conversion de l'énergie solaire incidente en électricité par les cellules photovoltaïques est limitée et la présence de poussière sur la surface des panneaux solaires affecte leur efficacité [1].

Pour remédier à cet effet négatif de la poussière, il est nécessaire de nettoyer régulièrement les panneaux solaires. Plusieurs techniques de nettoyage ont été proposées, notamment l'utilisation d'eau comme nettoyant, mais cette méthode a l'inconvénient de nécessiter une grande quantité d'eau [2-4].

Une nouvelle technique de nettoyage basée sur un phénomène électrostatique utilisant la décharge couronne a été développée pour améliorer l'efficacité de rendement des panneaux photovoltaïques. Cette technique consiste à utiliser des fils alimentés en haute tension pour générer un flux de vent ionique qui nettoie la surface du panneau.

2. Matériel

2.1 Matériel utilisé:

- Panneau photovoltaïque
- Source d'alimentation CC haute tension
- Dispositif de nettoyage
- Hygromètre
- Anémomètre
- Ampèremètre
- l'appareil Nettoyeur
- Véhicule.

2.2 Méthodes

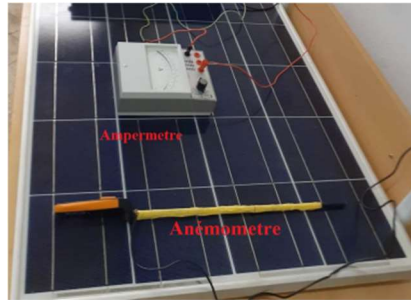
Ce travail de recherche a consisté à tester les capacités de nettoyage d'un appareil produisant un vent ionique. Pour cela, un système expérimental a été mis en place pour mesurer les caractéristiques de courant, de vitesse et de puissance de cet appareil.

La figure 1(a) présente une photographie de l'appareil nettoyeur, qui est composé d'une carcasse contenant deux électrodes: une électrode active sous forme de fil reliée à une haute tension et une électrode collectrice sous forme de rectangle en aluminium reliée à la terre.

La carcasse en FOREX sert à isoler électriquement les électrodes et à les fixer. L'appareil est entraîné par un véhicule contrôlé par une carte ARDUINO et est placé au-dessus d'un panneau photovoltaïque pour assurer son nettoyage dès le premier passage.



(a)



(b)

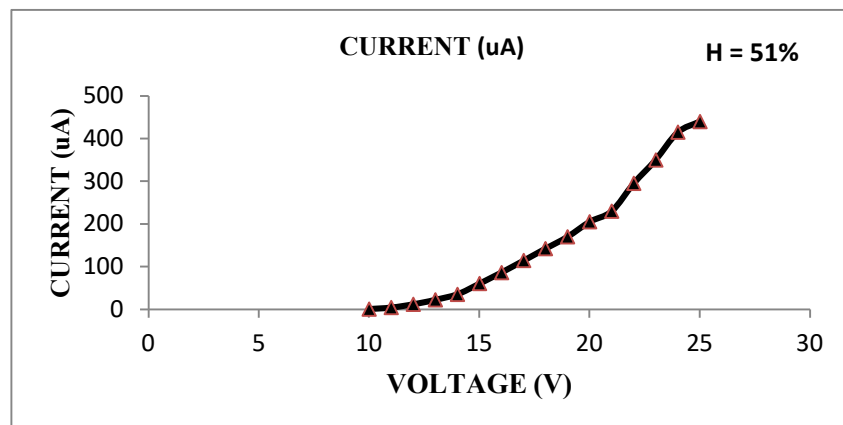


(c)

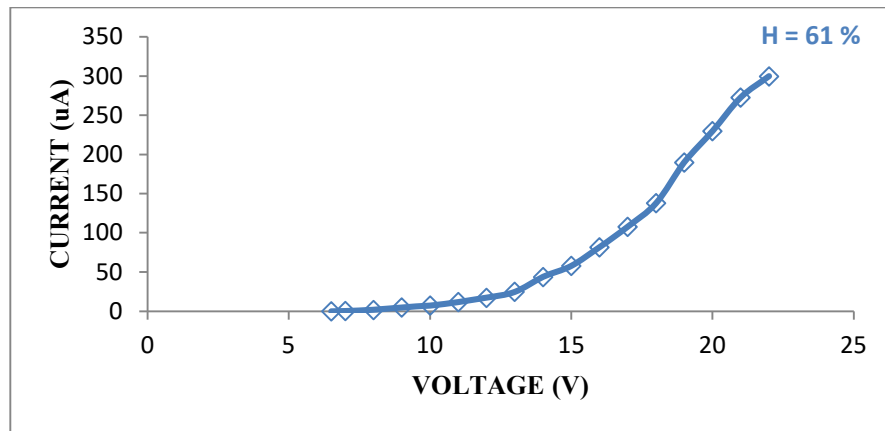
La figure 1: l'appareil nettoyeur et matériel utilisé, (a):l'appareil nettoyeur , (b):Ampèremètre + Anémomètre, (c):source d'alimentation haute tension

3. Résultat:

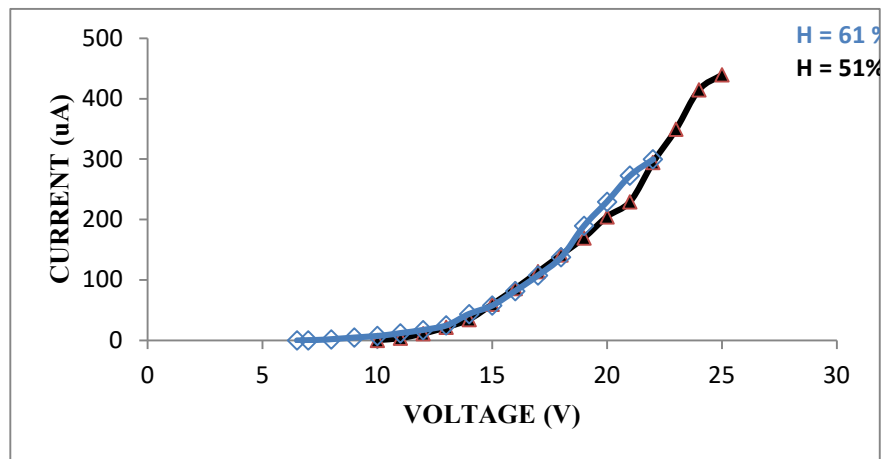
3.1 Résultat de l'humidité



La figure 2. La variation du courant en fonction de la tension avec humidité différentes H=51%

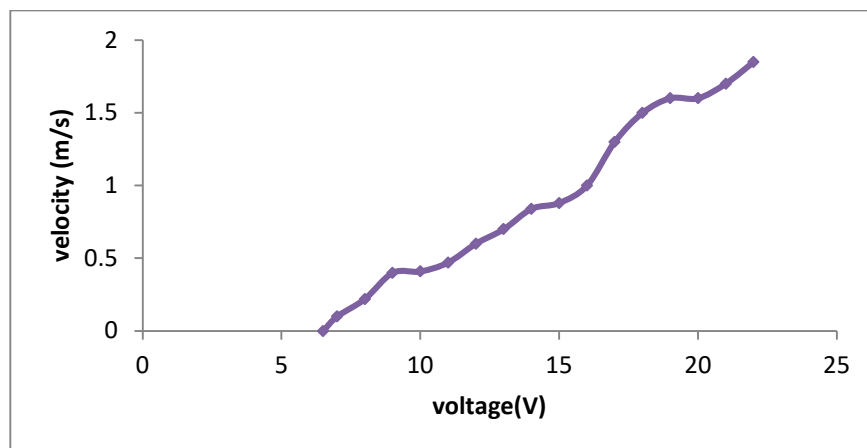


La figure 3. La variation du courant en fonction de la tension avec humidité différentes H=61%



La figure4. La variation du courant en fonction de la tension avec humidité différentes H=51% et H= 61%

3.1 Résultat de la vitesse du vent ionique



La figure5. La variation de la vitesse du vent en fonction de tension

4. Discussion

En se basant sur les différentes figures obtenues, les observations suivantes ont été faites :

Le courant consommé par le dispositif de nettoyage augmente en fonction de l'augmentation de la tension, depuis la tension d'apparition jusqu'à la tension de claquage.

4.1 Variation de l'humidité

La tension d'apparition du phénomène de décharge couronne et la tension de claquage varie légèrement en fonction du taux d'humidité. Pour un taux d'humidité de 51 % (voir figure 2), la tension d'apparition de la décharge couronne est de 10 kV avec une consommation de courant de 0,5 μ A et la tension de claquage est de 25 kV avec une consommation de courant de 440 μ A, tandis que pour un taux d'humidité de 61 % (voir figure 3), la tension d'apparition est de 6.5 kV avec une consommation de courant de 0,1 μ A et la tension de claquage est de 22 kV avec une consommation de courant de 300 μ A.

4.2 Variation de La vitesse du vent ionique

La vitesse du vent ionique augmente à mesure que la tension de la décharge couronne augmente jusqu'à une valeur proche de la tension de claquage, et en fonction du courant, la meilleure valeur pour le vent ionique est de 1,9 m/s pour une tension de 25 kV et un courant de 420 μ A, avec une consommation de 11 W. En utilisant les paramètres optimaux de la configuration étudiée, le nettoyage des panneaux photovoltaïques par décharge couronne peut atteindre une efficacité de nettoyage allant jusqu'à 95%.

5. Conclusion

Ce travail présente une nouvelle méthode pour nettoyer les panneaux photovoltaïques. Les résultats de cette étude montrent que le dispositif proposé

peut générer un vent ionique important de 2m/sec avec une consommation d'énergie de seulement 11 W. Ces caractéristiques de courant et de vent ionique peuvent être utilisées pour développer des configurations plus performantes et améliorer l'efficacité du nettoyage.

Références

- [1] W. Javed, Y. Wubulikasimu, B. Figgis, B. Guo, Characterization of dust accumulated on photovoltaic panels in Doha, Qatar, *Sol. Energy* 142 (2017) 123–135.
- [2] Saravanan, S. & Darvekar, K. S. Solar Photovoltaic Panels Cleaning Methods A Review. *International Journal of Pure and Applied Mathematics*, 118(24), 1–17. (2018).
- [3] K. Ilse, L. Micheli, B. W. Figgis, K. Lange, D. Daßler, H. Hanifi, F. Wolfertstetter, V. Naumann, C. Hagedorf, R. Gottschalg, J. Bagdahn, Techno-economic assessment of soiling losses and mitigation strategies for solar power generation. *Joule* 3, 2303–2321 (2019)
- [4] R. K. Jones, A. Baras, A. Al Saeeri, A. AlQahtani, A. O. Al Amoudi, Y. Al Shaya, M. Alodan, S. A. Al-Hsaien, Optimized cleaning cost and schedule based on observed soiling conditions for photovoltaic plants in Central Saudi Arabia. *IEEE J. Photovoltaics*. 6, 730–738 (2016).



Acoustic characterization of superconductor material Pr123

¹N. Sayoud^{1*}

Department of Physics, Faculty of science, Badji Mokhtar University, Annaba 23000, Algeria

* Corresponding author: E-mail address: nawalphysique@yahoo.fr

DOI : <https://doi.org/10.58452/jpcr.v2i2.162>

Article history

Received April 29, 2023

Accepted for publication October 18, 2023

Abstract

Our study consisted in the characterization of the superconducting material Pr123 using the acoustic method and the non destructive testing (NDT). Our work was performed at high working frequency of 600MHz. We studied the superconducting bulk system with the use of a coupling fluid to obtain propagation modes. The determination of these modes according to the Brekhovskikh model and the modeling of the reflection coefficient $R(\theta)$ and the acoustic signature $V(z)$, allows us to determine the moduli of elasticity of the studied superconducting material: Young's modulus (E) and shear modulus (G) in order to determine the critical angles: longitudinal (θ_L), transverse (θ_T) and Rayleigh critical angle (θ_R) which correspond respectively to the longitudinal acoustic wave, the transverse acoustic wave and the Rayleigh acoustic wave propagating in the superconducting material Pr123.

Keywords: Superconducting material, mechanical properties, acoustic signature $V(z)$, reflection coefficient $R(\theta)$, Young' modulus.

1. Introduction

Superconducting materials have properties of conducting electric current without any resistance at very low temperatures near absolute zero [1-3]. These materials are used in many fields such as medical and military...etc. This use requires the characterization and quantification of the mechanical properties of this type of materials. Therefore, our study consists in the characterization of the superconducting material Pr123, by acoustic techniques or ultrasonic method because of their non-destructive aspect (NDT). Our study was done at high working frequency of 600MHz and with the use of a coupling liquid.

2. Method

The acoustic microscope is a characterization device that consists of four distinct parts. In an acoustic microscope, the part of emission and reception of the acoustic wave represents the acoustic part. It is essentially composed of a sensor, the delay line and the acoustic lens.

In the case of a massive material, liquid-substrate system, the expression reflection coefficient was given by a calculation method, using the mechanical balance, the continuity of stresses and displacements at the interface, was developed by Brekhovskikh [4] :

$$R(\theta) = \frac{Z_L \cos^2 2 \theta_T + Z_T \sin^2 2 \theta_T - Z_0}{Z_L \cos^2 2 \theta_T + Z_T \sin^2 2 \theta_T + Z_0} \quad (1)$$

where Z_L and Z_T are respectively the longitudinal and transverse acoustic impedances of the solid. Z_0 is the acoustic impedance of liquid.

The expression for the acoustic signature $V(z)$ is of the form [4]:

$$V(z) = \int_0^{\theta_{max}} p^2(\theta) R(\theta) \exp(2jk_0 z \cos \theta) \sin \theta \cos \theta d\theta \quad (2)$$

Where z is the defocusing of the sensor.

The acoustic signature $V(z)$ is formed by periodic signals. The periodicity Δz of the interference gives information about the surface acoustic wave, this periodicity calculated by Bertoni is of the form:

$$\Delta z = \frac{V_{Liq}}{2f(1 - \cos R)} \quad (3)$$

The different moduli of elasticity are: the Young's modulus (E), the shear modulus (G), the bulk modulus (B). These moduli can be determined according to the following relationships:

$$G = \rho V_T^2 \quad (4)$$

$$E = 2G(1 + \nu) \quad (5)$$

$$B = \frac{E}{3(1-2\nu)} \quad (6)$$

3. Results

The results of the modeling of the reflection coefficient (modulus and phase) that we obtained for the system: methanol-Pr123 are presented in the figures 1, 2. From the modulus (figure 1) we obtained the longitudinal critical angle θ_L and the transverse critical angle θ_T . And from the phase (figure 2) we obtained the critical angle of Rayleigh θ_R . The results are grouped in table 1.

The determination of the critical angles of the propagating waves, (longitudinal, transverse and Rayleigh) from the amplitude and phase of $R(\theta)$, allows us to determine the different velocities of the modes that propagate in this material superconductor according to the Snell-Descart law. The results obtained are summarized in table 2.

The results of the acoustic signature $V(z)$ and its FFT that we obtained for the considered system are presented in the figures 3, 4.

The results that we have obtained, of the different elastic moduli of the studied superconducting material are summarized in table 3.

4. Discussion

The curves in the figure 3 show that the acoustic signature $V(z)$ is formed by periodic signals Δz . The determination of the periodicity Δz , allows us to deduce the different velocities of the modes propagating in the superconducting material.

The elastic constants of a superconducting material (E, G and B) can be determined by various experimental methods. Among these methods is the ultrasonic technique which gives similar results to those obtained by other investigative techniques. However, the ultrasonic method, which is based on the propagation of acoustic waves generated at high frequency, is a non-destructive method, unlike the so-called classical techniques.

The obtained results of the elastic moduli of the studied material are in good agreement with those of the literature [5].

Figures and Tables

Figures

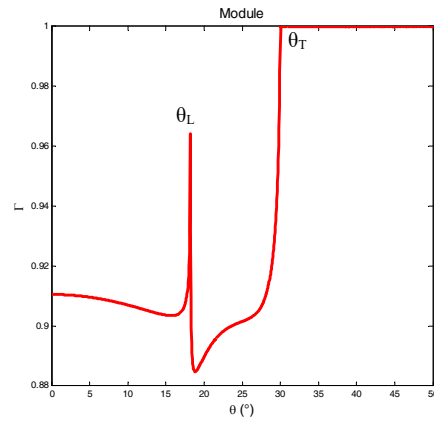


Figure 1: Modulus of the reflection coefficient of Pr123.

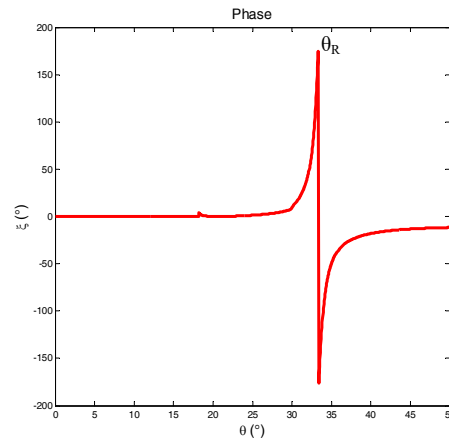


Figure 2: Phase of the reflection coefficient of Pr123.

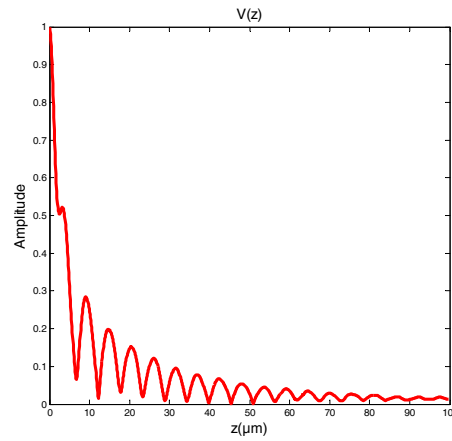


Figure 3: Acoustic signature $V(z)$ of Pr123.

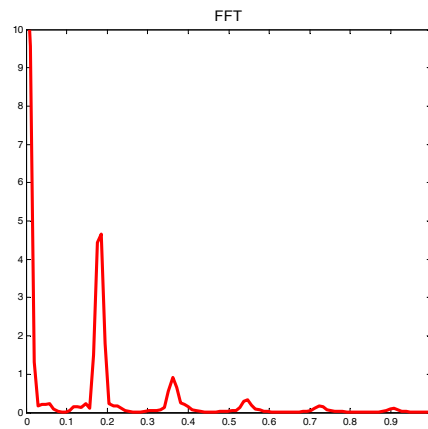


Figure 4: FFT of the acoustic of Pr123.

Tables

Table 1. The critical longitudinal, transverse and Rayleigh angles.

θ_L (°)	θ_T (°)	θ_R (°)
18.2229	9.8333	3.5

Table 2. The velocities of the propagation modes in Pr123.

V_L (m/s)	V_T (m/s)	V_R (m/s)
3479.742177	3119.79	0.7

Table 3. Elastic moduli of the studied superconducting material.

E(GPa)	E_{ii}(GPa)	G(GPa)	G_{iii}(GPa)	B(GPa)
59.19	59.4	[5]	25.1325 [5]	30.60

5. Conclusion

The acoustic method used allowed us to characterize the superconducting materials and to determine their mechanical properties.

The results obtained concerning the elastic moduli of the studied material are in good agreement with the experimental results quoted in the literature, which testifies to the validity of the proposed homogenization method.

References

- [1] N. A. Rasih, A. K. Yahya. Journal of Alloys and Compounds 480, (2009).pp.777-781.
- [2] Boyang Shen et al. doi.org/10.3390/electronics 11071098. (2022).
- [3] X. Ling Yan et al. J. Materials, 11, 293; doi: 10.3390/ma11020293. 2018.
- [4] N. Sayoud et al. Journal of Physics: Conf. Series 1017 (2018).
- [5] R. G. Munro. 20899. NISTIR 6853, (2002).



DFT study of the electronic and optical properties of ternary alkali metal tetrafluoridobromates materials ABrF_4 (A=Na, K and Rb)

Ishak Mebarkia^{1*}

¹ Applied optics laboratory, Institute of Optics and Precision Mechanics, Ferhat Abbas University Setif 1, Setif, 19000, Algeria.

* Corresponding author: Tel.: +213 657308527; E-mail: ishak.mebarkia@univ-setif.dz
DOI : <https://doi.org/10.58452/jpcr.v2i2.165>

Article history

Received April 30, 2023

Accepted for publication December 2, 2023

Abstract

This work deals with a theoretical investigation of structural, electronic, and optical properties of alkali metal tetrafluoridobromates materials that crystallize in tetragonal structure (NaBrF_4 , KBrF_4 , and RbBrF_4) using the Density Functional Theory (DFT) within the pseudo-potential plane-wave approach as implemented in Cambridge Serial Total Energy Package (CASTEP) code. The structural parameters are in good agreement compared to the experimental values stated in the literature. The calculated electronic properties indicate that these ternary compounds are wide bandgap semiconductor materials. NaBrF_4 is a semiconductor compound with a direct band gap, whereas, KBrF_4 and RbBrF_4 are semiconductor compounds together with an indirect band gap. The main optical parameters are studied in detail. The large optical absorption range in the ultraviolet (UV) region suggests that these semiconductor materials could be helpful for specific implementations in UV optoelectronic devices; therefore, this theoretical investigation is probable to motivate future experimental works.

Keywords: ABrF_4 , alkali metal tetrafluoridobromates, DFT, electronic properties, optical properties, semiconductor materials.

1. Introduction

The alkali metal fluorides family has many characteristics desirable for optoelectronic properties, such as wide bandgaps, large absorption in the UV region, and lower refractive indices compared to those of oxides[1]. Our studied materials are ternary compounds belonging to the same crystalline structure and sharing one of the alkali elements such that Sodium "Na", Potassium "K", and Rubidium "Rb" as a cation with an anion formed by Bromine bonded with four Fluorine "BrF₄" [2,3]. To the best of our knowledge, no theoretical nor experimental studies of the electronic, and optical properties have been carried out on the herein-studied compounds except our recent theoretical investigation using a different exchange-correlation function (Perdew-Burke-Ernzerhof for solids (PBE-sol))[4]. The results presented in this work may be useful in evaluating potential technological applications of NaBrF₄, KBrF₄, and RbBrF₄ materials.

2. Method of calculations

To carry out our first-principle calculations, we employed the density functional theory (DFT) framework and utilized the Cambridge Serial Total Energy Package (CASTEP) code[5]. Our method relied on the pseudopotential plane-wave (PP-PW) approach. For the electronic exchange potential, we applied the Wu-Cohen (WC) exchange-correlation function, which was specifically designed for solids and followed the generalized gradient approximation (GGA)[6]. The energy cut-off for the basis set of plane-waves used was 60 Ry. The Monkhorst-Pack special k-point sampling was used to cover the Brillouin zone (BZ) with a mesh of 4×4×2, which is equivalent to 3 irreducible points within the first BZ [7].

3. Results

The structure of ABrF₄ (A=Na, K and Rb) ternary compounds is tetragonal space group I4/mcm (No. 140) as shown in Figure 1, where the unit cell contains four formula units (Z=4) in which the atoms are positioned in the following Wyckoff sites: A: 4a(0; 0; ¼), Br: 4d(½; 0; 0), and F: 16l(x_F; y_F; z_F). To determine the equilibrium structural parameters including the lattice parameters (a and c) and the internal coordinates of Fluorine atom (x_F, y_F, and z_F), we applied different values of hydrostatic pressures and for each value we calculated the volume V and its total energy E. Thereafter, we extract the different equilibrium parameters, according to the equilibrium volume V₀, which is corresponding to the minimum value of the ground state energy E₀.

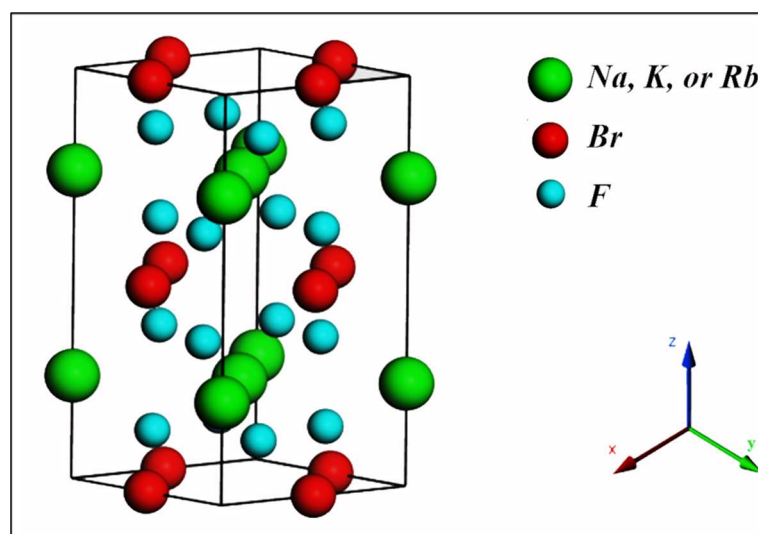


Figure 1. Crystal structure of $ABrF_4$ ($A=Na, K$ and Rb) ternary compounds.

Furthermore, The calculated cell volumes V at fixed applied hydrostatic pressures and the associated total energies E were fitted to the following Birch-Murnaghan isothermal equation of states (BMEOS) [8], to obtain the bulk modulus B_0 and its pressure derivative B'_0 , as shown in Figure 2.

$$E(V) = E_0 + \frac{9V_0B_0}{16} \left\{ \left[\left(\frac{V_0}{V} \right)^{\frac{2}{3}} - 1 \right]^3 B'_0 + \left[\left(\frac{V_0}{V} \right)^{\frac{2}{3}} - 1 \right]^2 \left[6 - 4 \left(\frac{V_0}{V} \right)^{\frac{2}{3}} \right] \right\} \quad (1)$$

where E_0 and V_0 are the energy and volume at zero pressure, respectively. Table 1 displays the computed ground states parameters such as the lattice constants a and c , the internal coordinates of Fluorine atom x_F , y_F , and z_F , the Bulk modulus B_0 and its pressure derivative B' along with the experimental data, as well as the other theoretical calculations for comparison. We can notice that there is an excellent agreement between our calculated results and the experimental ones for all studied compounds which affirms the reliability of our computations in this work.

The electronic band structure along the Brillouin zone high symmetry lines is shown in Figure 3 for $ABrF_4$ ($A= Na, K$, and Rb) ternary compound. The Fermi level E_F positioned at 0 eV and indicated by the horizontal dashed line. The calculated values of the energy gap are 3.006 eV, 3.180 eV, and 3.222 eV for $NaBrF_4$, $KBrF_4$, and $RbBrF_4$, respectively, which gives these materials the characteristic to become semiconductors with wide band gaps. Furthermore, it is clear from the forms of electronic structure that $NaBrF_4$ has a direct band gap, owing to its VBM and its CBM are located at Γ point, while the other studied compounds have an indirect band gap, which their VBM are situated near

the point Γ in the Γ -X orientation, and their CBM situated at the Γ point.

Table 1. The lattice constants a and c (in Å), the internal coordinates of Fluorine atom x_F, y_F and z_F , the Bulk modulus B_0 and its pressure derivative B_0' of $ABrF_4$ ($A = Na, K$ and Rb) materials.

materials	Parameters	calc.	other calc.	Expt.
NaBrF ₄	a	5.792	5.546 ^d , 5.788 ^{c,m} 5.7814 ^f	5.762 ^a , 5.7848 ^b , 5.7239 ^c
	c	10.432	10.09 ^d , 10.44 ^c , 10.4294 ^f	10.327 ^a , 10.400 ^b , 10.331 ^c
	x_F	0.3346	0.33452 ^f	0.6633 ^b , 0.33524 ^c
	y_F	0.1653	0.16548 ^f	-0.1633 ^b , 0.16476 ^c
	z_F	0.1312	0.13140 ^f	0.1299 ^b , 0.13080 ^c
	B_0	28.683	28.09621 ^f	/
	B_0'		6.89523 ^f	/
	KBrF ₄	a	6.183	6.1769 ^f
c		11.170	11.1626 ^f	11.108 ^a , 11.081 ^g , 11.103 ^h , 11.1 ⁱ , 11.0509 ^j
x_F		0.6542	0.65585 ^f	0.161 ^g , 0.152 ^h , 0.152 ⁱ , 0.65508 ^j
y_F		0.1533	0.15585 ^f	0.661 ^g , 0.652 ^h , 0.652 ⁱ , 0.15508 ^j
z_F		0.3777	0.37835 ^f	0.147 ^g , 0.880 ^h , 0.121 ⁱ , 0.37889 ^j
B_0		19.225	20.42155 ^f	/
B_0'		6.5501	6.42551 ^f	/
RbBrF ₄		a	6.446	6.20 ⁿ , 6.94 ^o , 6.3895 ^f
	c	11.612	11.74 ⁿ , 8.93 ^o , 11.5819 ^f	11.1538 ^a , 11.489 ^k , 11.4934 ^l , 11.4659 ^m
	x_F	0.6499	0.154 ⁿ , 0.1458 ^o , 0.6508 ^f	0.1490 ^k , 0.151 ^l , 0.6501 ^m
	y_F	0.1498	-0.346 ⁿ , -0.3542 ^o , 0.1508 ^f	-0.3510 ^k , -0.349 ^l , 0.1501 ^m
	z_F	0.6087	0.1145 ⁿ , 0.1411 ^o , 0.6171 ^f	0.1162 ^k , 0.1193 ^l , 0.61660 ^m
	B_0	17.634	18.27326 ^f	/
	B_0'	7.0203	6.75771 ^f	/

Note: ^aRef.[9], ^{b,c,d,e}Ref.[10], ^fRef.[4], ^gRef.[11], ^hRef.[12], ⁱRef.[13], ^jRef.[14], ^kRef.[15], ^{l,n,o}Ref.[16], ^mRef.[17].

The main optical parameters such as the refractive index n and the absorption coefficient α that describe the optical behaviour of the material when it interacts with an external electromagnetic field can be computed from the dielectric permittivity ϵ , which is a complex function depends of the angular frequency ω of the applied electric field, given as:

$$\epsilon(\omega) = \epsilon_1(\omega) + i \epsilon_2(\omega) \quad (2)$$

where ϵ_1 and ϵ_2 are respectively the real and imaginary parts of the dielectric function.

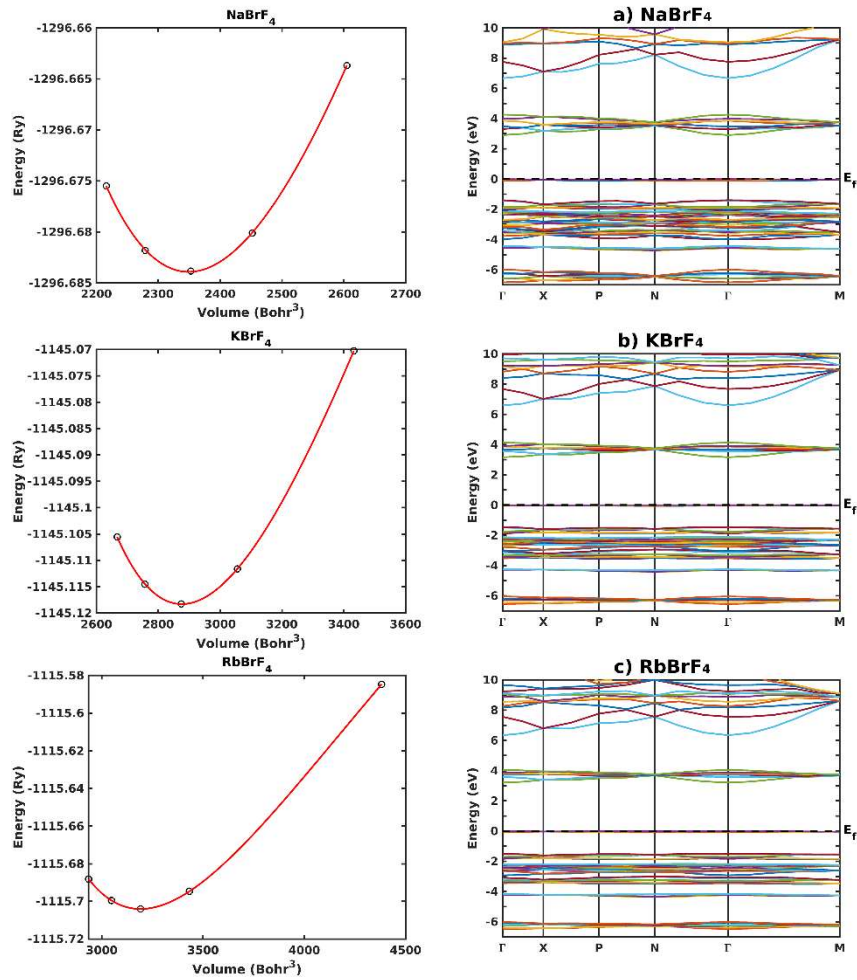


Figure 2. The total energy Bohr versus cell volume data. The black circles are the structure of $ABrF_4$ ($A = Na, K$ and Rb) calculated results and the red lines ternary alkali metal tetrafluoride-bromates materials represent the BMEOS fits.

As $ABrF_4$ ($A = Na, K$ and Rb) ternary compounds crystallize in the tetragonal structure, the optical spectra of the dielectric function ϵ_1 and ϵ_2 , the refractive index n and the absorption coefficient α are plotted in Figure 4 and Figure 5 for only two components indicating by the superscripts xx and zz , which concerning the polarization of the applied electric field along the x (or y) and z directions, respectively.

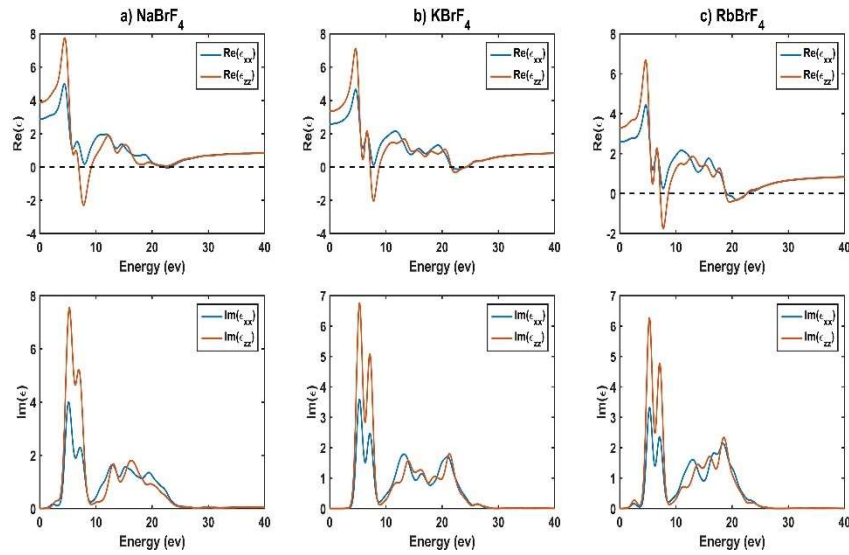


Figure 4. The spectra of the real and imaginary parts of the dielectric function for $A\text{BrF}_4$ ($A=\text{Na}, \text{K}$ and Rb) ternary compounds.

It is clear from the different optical spectra that the polarized components are not identical when the energy less than 25 eV, indicating that these materials having an optical anisotropy behavior in this energy region. According to the spectra of the real part ϵ_1 (called also the dispersive part) we can affirm that the herein studied compound shows a Drude like behavior, which ϵ_1 crosses the zero frequency and represents the dielectric response to a static electric field. The calculated values of the zero-frequency limit for the different polarized components ($\epsilon_1^{xx}(0)$ and $\epsilon_1^{zz}(0)$) are mentioned in Table 2. Furthermore, we can notice that ϵ_1^{zz} is the dominant component owing to its prominent peak located at around 4.7 eV, 4.8 eV, and 4.9 eV for NaBrF_4 , KBrF_4 , and RbBrF_4 , respectively.

Table 2. The calculated values of the static dielectric constant $\epsilon_1(0)$, the energy values correspond to the maximum peaks of $\epsilon_2(\omega)$, and the static refractive index $n(0)$.

Compounds	$\epsilon_1^{xx}(0)$	$\epsilon_1^{zz}(0)$	$\epsilon_2^{xx}(\omega)$	$\epsilon_2^{zz}(\omega)$	$n^{xx}(0)$	$n^{zz}(0)$
NaBrF_4	2.77	3.70	5.50	5.11	1.68	1.95
KBrF_4	2.43	3.24	5.81	5.14	1.61	1.83
RbBrF_4	2.22	3.15	5.92	5.22	1.60	1.82

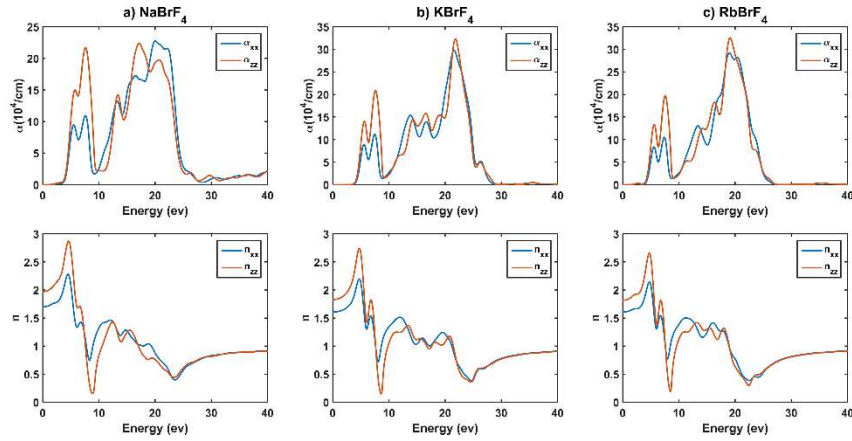


Figure 5. The absorption spectrum and the refractive index profile of $ABrF_4$ ($A=Na, K$ and Rb) materials.

As shown in Figure 5, the refractive index profile n takes the shape of the dispersive part spectrum ϵ_1 , where n^{zz} is the dominant component of the refractive index that possess a significant peak situated at about 4.8 eV, 4.9 eV, and 5.0 eV for $NaBrF_4$, $KBrF_4$, and $RbBrF_4$, respectively. Moreover, the obtained values of the static refractive index for the different polarized components ($n^{xx}(0)$ and $n^{zz}(0)$) are mentioned in Table2, which are close to the values obtained by the following semi-empirical relation:

$$n(0) = \sqrt{\epsilon_1(0)} \quad (3)$$

These consequences confirm the reliability of the obtained results for $ABrF_4$ ($A = Na, K$ and Rb) ternary compounds.

The imaginary part of the dielectric function ϵ_2 (called also the absorptive part) shows an anisotropy between its polarized components, where ϵ_2^{xx} and ϵ_2^{zz} have prominent peaks at the lower energy region. The energy values correspond to these peaks mentioned in Table2, which principally originate from the optical transition between the highest occupied valence band and the lowest unoccupied conduction band.

As mentioned in Figure 5, the absorption profile α takes the shape of the absorptive part spectrum ϵ_2 , where represents the maximum absorbance in the ultraviolet (UV) optical range, which the first main peak located at about 5.4 eV signifies that this ternary compound can be used for producing specified UV optoelectronic devices. Furthermore, the absorption thresholds situated at 3.0 eV, 3.2 eV, and 3.3 eV for $NaBrF_4$, $KBrF_4$, and $RbBrF_4$, respectively. These results confirm the reliability of the obtained energy gap results for these semiconductors.

4. Conclusion

In this study, the electronic and optical properties of $A\text{BrF}_4$ ($A = \text{Na}, \text{K}$ and Rb) materials were investigated in details using the pseudopotential plane wave method within the generalized gradient approximation as enhanced by Wu and Cohen. Our calculated equilibrium structural parameters agree well with the other available results of the literature. Based on the results of electronic properties, it can be concluded that these ternary compounds are semiconductor materials, NaBrF_4 has a direct band gap, whereas, KBrF_4 and RbBrF_4 have an indirect band gap. The outcome of our investigation in the optical properties suggests that these semiconductors could be useful materials for specific applications in UV optoelectronic devices owing to their wide absorption in the UV region. Finally, our results can be considered as a source for future experimental research works.

References

- [1] A.J. Stevenson, H. Serier-Brault, P. Gredin, M. Mortier. *J. Fluor. Chem.* 132 (2011) 1165–1173.
- [2] O. Materials. *Optical & Wiley Series in Materials for Electronic and Optoelectronic*, 2005.
- [3] R. Burkhalter, I. Dohnke, J. Hulliger. 2001.
- [4] I. Mebarkia, A. Manallah, R. Belghit. *Phys. B Condens. Matter.* 624 (2022) 413450.
- [5] S.J. Clark, M.D. Segall, C.J. Pickard, P.J. Hasnip, M.I.J. Probert, K. Refson, M.C. Payne. *Zeitschrift Fur Krist.* 220 (2005) 567–570.
- [6] Z. Wu, R.E. Cohen. *Phys. Rev. B - Condens. Matter Mater. Phys.* 73 (2006).
- [7] Hendrik J Monkhorst, J.D. Pack. *Phys. Rev. B.* 13 (1976) 5188–5192.
- [8] F. Birch. *Phys. Rev.* 71 (1947) 809–824.
- [9] A.I. Popov, Y.M. Kiselev, V.F. Sukhoverkhov, N.A. Chumaevskij, O.A. Krasnyanskaya, A.T. Sadikova. *Zh. Neorg. Khim.*; 32:5 (1987).
- [10] S.I. Ivlev, R. V. Ostvald, F. Kraus. *Monatshefte Fur Chemie.* 147 (2016) 1661–1668.
- [11] S. Siegel. *Acta Crystallogr.* 9 (1956) 493–495.
- [12] W.G. Sly, R.E. Marsh. *Acta Crystallogr.* 10 (1957) 378–379.
- [13] A.J. Edwards, G.R. Jones. *J. Chem. Soc. A Inorganic, Phys. Theor. Chem.* (1969) 1936–1938.
- [14] S.I. Ivlev, F. Kraus. *IUCrData.* 3 (2018).
- [15] A.R. Mahjoub, A. Hoser, J. Fuchs, K. Seppelt. *Angew. Chemie.* 101 (1989) 1528–1529.
- [16] S.I. Ivlev, A.J. Karttunen, R. Ostvald, F. Kraus. *Zeitschrift Fur Anorg. Und Allg. Chemie.* 641 (2015) 2593–2598.
- [17] A. V. Malin, S.I. Ivlev, R. V. Ostvald, F. Kraus. *IUCrData.* 4 (2019).



L₁ sub-shell fluorescence yield for lanthanide elements with $58 \leq Z \leq 71$

K. Meddouh^{1,2*}, A. Kahoul^{1,2}, S. Daoudi^{1,2}, J.M. Sampaio^{3,4}, J.P. Marques^{3,4}, F. Parente^{4,5}, A. Hamidani^{1,2}, N.Kup Aylikci⁶, V. Aylikci⁷ and Y. Kasri⁸

¹Department of Matter Sciences, Faculty of Sciences and Technology, Mohamed El Bachir El Ibrahimi University, Bordj-Bou-Argeridj 34030, Algeria.

²Laboratory of Materials Physics, Radiation and Nanostructures (LPMRN), University of Mohamed El Bachir El Ibrahimi, Bordj-Bou-Argeridj 34030, Algeria.

³LIP – Laboratório de Instrumentação e Física Experimental de Partículas, Av. Prof. Gama Pinto 2, 1649-003 Lisboa, Portugal.

⁴Faculdade de Ciências da Universidade de Lisboa, Campo Grande, C8, 1749-016 Lisboa, Portugal.

⁵Laboratory of Instrumentation, Biomedical Engineering and Radiation Physics (LIBPhys-UNL), Department of Physics, NOVA School of Science and Technology, NOVA University Lisbon, 2829-516 Caparica, Portugal.

⁶Department of Energy Systems Engineering, Faculty of Engineering and Natural Sciences, Iskenderun Technical University, 31200 Iskenderun, Hatay, Turkey.

⁷Department of Metallurgical and Materials Engineering, Faculty of Engineering and Natural Sciences, Iskenderun Technical University, 31200 Iskenderun, Hatay, Turkey.

⁸Theoretical Physics Laboratory, Physics Department, University of Bejaia, 06000 Bejaia, Algeria.

^{*} Corresponding author. Tel./Fax (+213) 035862230.

E-mail address: kaouther.meddouh@univ-bba.dz

DOI: <https://doi.org/10.58452/jpcr.v2i2.168>

Article history

Received May 10, 2023

Accepted for publication December 04, 2023

Abstract

The lanthanides comprise the largest naturally occurring group in the periodic table, the “rare earth elements” which group the fourteen elements from 58Ce to 71Lu, which are also electropositive and reactive metals, except for yttrium. The researchers used these elements and calculated the yield of fluorescence (ω_{L1}) by theoretical, experimental and analytical methods due to the large number of their

Special Issue of the National Seminar of physics, Chemistry and their Applications “NSPCA’23”
March 6-7th, 2023, Mohamed El Bachir El Ibrahimi University, Bordj-Bou-Argeridj, Algeria.

applications in various fields of physical chemistry and medical research. In the present work, all the experimental L_1 sub-shell fluorescence yields taken from distinctive sources are studied. A detailed analysis of these data, and a table with weighted average values (ω_{L1W}) of these parameters are presented. New recommended values (ω_{WR}) are obtained dividing the experimental ratios (ω_{exp}) by the weighted ratios (ω_w) and removing out-of-range values (less than 0.8 or greater than 1.2). At that point, new values of average fluorescence yields were deduced using an interpolation that involves the well-known analytical function $[\omega_{Li-} / (1 - \omega_{Li-WR})]^{1/4}$ as function of the atomic number Z , and then semi-empirical data were deduced by fitting the ratio $R = \frac{\omega_{Li-exp}}{\omega_{Li-W}}$, for the three shells. A comparison was made with other theoretical, experimental, and empirical values reported in the literature. An evident correlation was observed between our result and other works.

Keywords: X-rays, atomic fundamental parameters fluorescence yields, recommended weighted average values, semi-empirical calculation.

I. INTRODUCTION

X-ray fluorescence parameters “fluorescence yields, production cross-sections, and intensity ratios ...” has a great important for increasing need for analysis of new materials. These parameters are required in many applications apart from the atomic physics studies including the surface chemical analysis, dosimetric computations for health physics, cancer therapy and industrial irradiation processing. In the past, several attempts were made to calculate the L_i ($i=1,2,3$) sub-shell fluorescence yields using a theoretical model, or by fitting the experimental data (empirical and semi-empirical formulae) for a wide range of elements. In this paper, it was focused on the L_1 sub-shell fluorescence yields and the deduction and improvement of their semi-empirical values for $58 \leq Z \leq 71$.

II. COMPUTATIONAL METHOD

The reported experimental values of the compiled L_i sub-shell fluorescence yields were extracted from the referenced articles (432 values for L_1 sub-shell in the atomic range $80 \leq Z \leq 96$) were taken in a three to fourth-digit format with their associated errors. While reviewing this data, we noticed that some values are far from each other, so we used the weighted average values given by the following formula [1]:

$$\Omega_W = (\sum_{i=1}^N (\Delta(\omega_{exp})_i)^{-2})^{-1} \sum_{j=1}^N (\omega_{exp} / (\Delta(\omega_{exp})_i)^2) \quad (1)$$

Where $(\omega_{exp})_i$ represents the i^{th} experimental value, $\Delta(\omega_{exp})_i$ is the uncertainty of the i^{th} experimental value, and N indicates the number of experimental data points.

In order to obtain reliable semi-empirical values, we have calculated the ratio of the experimental fluorescence yields with respect to the weighted average value: $R = (\omega)_{\text{exp}} / (\omega)_W$ then we have plotted the ratio R against the atomic number Z , as shown in Figs. 1. After we examined the weighted average values, we found that most of the experimental data point's ω are centered around the weighted average value of all elements. However, some values are much dispersed compared to the weighted values, in particular for the heavy elements due to the large number of experimental data points in this region, and therefore the large number of references used to collect data, experimental methods and conditions. To obtain a reliable weighted average value and a good semi-empirical result, with sufficient data points, we included only the experimental data points for which the ratio S varies within the range of [0.8 - 1.2].

About 41 values outside the interval [0.8 - 1.2] have been removed. Therefore, using once again formula (1) new recommended weighted average values ω_{L-WR} have been obtained. These recommended weighted average values ω_{L-WR} were used to calculate the empirical L-shell fluorescence yields. The approximation $(\omega_{L-WR} / 1 - \omega_{L-WR})^{1/4}$ is presented as function of Z and plotted in Figure 2. Consequently, we used the following function for these interpolations:

$$(\omega_{Li-WR} / 1 - \omega_{L-WR})^{1/4} = f(Z) = \sum_{n=0}^3 a_n Z^n \quad (2)$$

with:

$$a_0 = 4,65542 \pm 24,82493, \quad a_1 = -0,21449 \pm 1,15888$$

$$a_2 = 0,00358 \pm 0,01799, \quad a_3 = -1,93045 \cdot 10^{-5} \pm 9,29352 \cdot 10^{-5}$$

For the determination of empirical L shell fluorescence yields, formula (2) can be rewritten as follows:

$$\omega_{Li \text{ emp}} = (f(Z) / 1 + f(Z))^4 \quad (3)$$

It must be emphasized that the fitting of formula (2) and the associated coefficients are only valid in the region of atomic number $80 \leq Z \leq 96$, and the extension out of this region might take an unpredictable course.

Finally for the determination of the average semi-empirical fluorescence yields, it is calculated using the two expressions (2) and (3) as:

$$\omega_{Li \text{ S-emp}} = f(Z) \cdot \omega_{Li \text{ emp}} \quad (4)$$

III. RESULTAT AND DISSCUSION

The present calculation of semi-empirical average L sub-shell fluorescence yields according to equation (4) for all elements in the region $58 \leq Z \leq 71$ is listed in Table 1. The theoretical values of Krause at al [2], the fitted results of Puri et a. [3], Campbell. [4], Sahnoun et al [5] and the experimental measurements of Bonzi and Badiger, [6] Bansal et al., [7] Kacal et al., [8] are also added in the same table. Because there are no experimental reported data for the element $_{61}\text{Pm}$ the value of element is not in this table. The empirical average L_i sub-shell fluorescence yields

obtained are compared with the results of Krause et al [2], the fitted results Puri et al. [3], Campbell [4], Sahnoun et al [5] Bonzi and Badiger, [6] Bansal et al., [7] and Kacal et al., [8] as a function of the atomic number Z and are shown in figure 3.

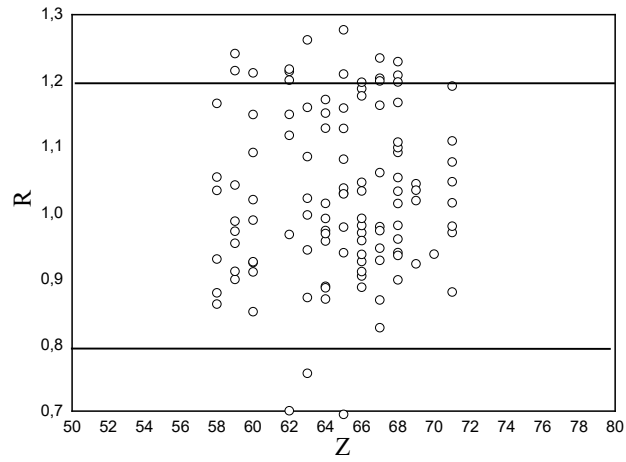


Fig. 1. The distribution of $R = (\omega)_{\text{exp}} / (\omega)_W$ for each reference from which the databases are extracted according to the atomic number Z .

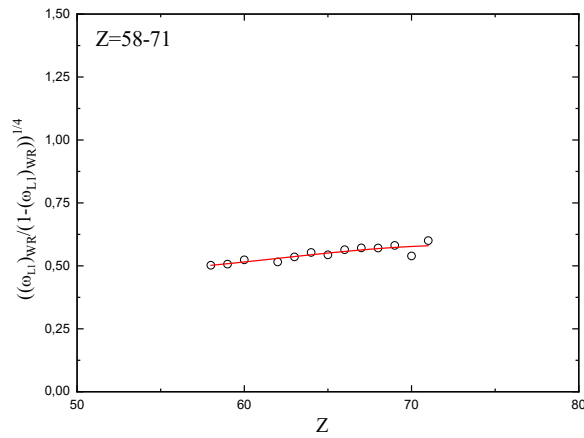


Fig. 2. Distribution of $(\omega_{L-WR} / 1 - \omega_{L-WR})^{1/4}$ as a function of atomic number Z .

TABLE I. SEMI-EMPIRICAL (THIS WORK), THEORETICAL, FITTED AND EXPERIMENTAL (OTHER WORKS) AVERAGE L SUB-SHELL FLUORESCENCE YIELDS FOR ALL ELEMENTS IN THE REGION $58 \leq Z \leq 71$.

Z-element	This work	Theo.	Fitt			Exp
	<i>Semi-Emp</i>	[2]	[3]	[4]	[5]	
Z = 58, Ce	0,0619	0,058	0,061	--	0,062	--
Z = 59, Pr	0,06772	0,061	0,065	--	0,0663	0,065[6]
Z = 60, Nd	0,07383	0,064	0,067	--	0,0706	--
Z = 61, Pm	0,08023	0,066	0,071	--	0,075	--
Z = 62, Sm	0,08688	0,071	0,075	0,075	0,0793	--
Z = 63, Eu	0,09376	0,015	0,078	0,08	0,0836	0,079[7]
Z = 64, Gd	0,10085	0,079	0,083	0,09	0,0879	0,085[7]
Z = 65, Tb	0,1081	0,083	0,087	0,1	0,0921	--
Z = 66, Dy	0,11549	0,089	0,091	0,1	0,0963	0,096[7]
Z = 67, Ho	0,12298	0,094	0,095	0,11	0,1004	0,0107[7]
Z = 68, Er	0,13052	0,1	0,105	0,12	0,1043	0,093[8]
Z = 69, Tm	0,13807	0,106	0,109	0,13	0,1081	--
Z = 70, Yb	0,14558	0,111	0,114	0,13	0,1118	--
Z = 71, Lu	0,15301	0,12	0,12	0,14	0,1153	0,0115[8]

In figure 1, agreement between our empirical L1 sub-shell fluorescence yields results and the theoretical, fitted and experimental values is good, especially in the range $58 \leq Z \leq 62$. In addition, our data differ in percentage with the theoretical values of Krause (1979) [2], the argument varies from 6.30% to 13.31% for the first three elements, and deviation varies from 17.73% to 23.75% for Z high. Where the relative difference (RD) between the obtained empirical values and other calculations were obtained using the expression $RD(\%) = \left| \frac{\omega - \omega_{emp}}{\omega_{emp}} \right| \times 100$. In what concerns the comparison with previous fitted results, our semi-empirical average L sub-shell fluorescence yields also agree with the values of Campbell.(2003) [4] within 5.8–14.67%, the agreement between other semi-empirical calculation and the fitted and experimental values are not satisfying. The observed deviation varies from 16.80% to 21.69% for Puri et al.(1994) [3] except for the five elements (the argument varies from 1.45% to 13.67%), 14.80% to 24.64% for Sahnoune et al.(2016) [5] except for the seven elements (the argument varies from 0.16% to 12.84%).

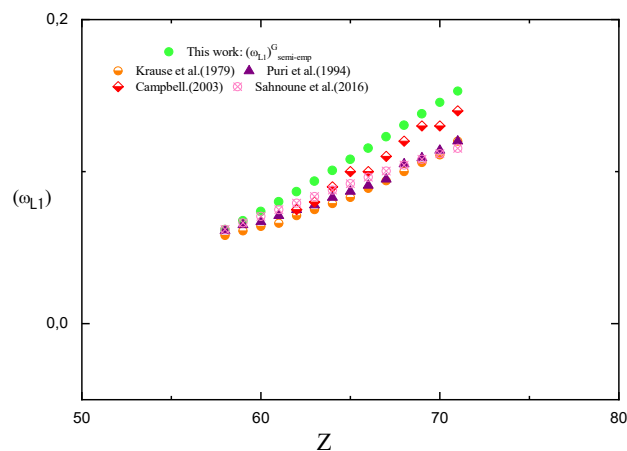


Fig. 3. The investigated semi-empirical L sub-shell fluorescence yields compared to their corresponding calculations Krause [2], Puri et a. [3], Campbell. [4], Sahnoune et al [5], Bonzi and Badiger, [6], Bansal et al., [7] and Kacal et al., [8] as a function of the atomic number Z .

IV. Conclusion

The average L sub-shell fluorescence yield measurements reported in the literature covering the period from 1934 to 2020 have been reviewed and presented in a table form (about 382 measurements). Using simple methods, a new set of L sub-shell fluorescence yields has been determined for elements in the atomic region $58 \leq Z \leq 71$. The deduced semi-empirical fluorescence yields are in a relatively good agreement with those of other groups for the whole range of atomic number. In addition to available experimental and theoretical average fluorescence yields, current values can be added to databases and made available to workers in the field of atomic inner layer ionization processes.

References

- [1] Allawadhi KL, Sood BS, MittalR, Singh N and Sharma JK 1996 X Ray Spectrom. 25, 233–238.
- [2] Krause, M.O., 1979. Atomic radiative and radiationless yields for K and L shells, J. Phys. Chem. Ref. Data 8, 307-327.
- [3] Puri, S., Mehta, D., Chand, B., Singh, N. Trehan, P.N., 1993. L-shell fluorescence yields and Coster-Kronig transition-probabilities for the elements with $25 \leq Z \leq 96$, X-ray Spectrom. 22, 358-361.
- [4] Campbell, J.L., 2003. Fluorescence Yields and Coster-Kronig probabilities for the atomic L Subshell. Atom. Data Nucl. Data Tables 85, 291-315.
- [5] Sahnoune, Y., Kahoul, A., Kasri, Y., Deghfel, B., Medjadi, D. E., Khalfallah, F., ... & Nekkab, M. (2016). L1, L2, and L3 subshell

fluorescence yields: Updated database and new empirical values. *Radiation Physics and Chemistry*, 125, 227-251.

- [6] Bonzi, E.V., Badiger, N.M., 2006. Measurement of L subshell fluorescence yields of elements in the range $45 \leq Z \leq 50$ using synchrotron radiation. *Nucl. Instr. Meth. B* 248, 242-246.
- [7] Bansal, H., Tiwari, M. K., & Mittal, R. (2017). L sub-shell fluorescence cross-section measurements for elements, $Z= 62-67$, at tuned photon energies. *Journal of Quantitative Spectroscopy and Radiative Transfer*, 199, 93-102.
- [8] Kacal, M.R., Han, I., Akman, F., Durak, R., 2012. Measurement of L subshell fluorescence yields for high-Z elements excited by 22.6 keV photons. *J. Quant. Spectr. Rad. Transf* 113, 373-3.



Agricultural Applications of Nanocomposites Superabsorbent Polymers: A Review

Mohammad Alrbaihat

Ministry of Education, Dubai, 3962, United Arab Emirates

** Corresponding author: Tel./Fax:; E-mail address: moh.irbeihat83@hotmail.com*

DOI: <https://doi.org/10.58452/jpcr.v2i2.166>

Article history

Received May 01, 2023

Accepted for publication October 16, 2023

Abstract

A superabsorbent polymer (SAP) can absorb large quantities of water. Hydrophilic materials are known as superabsorbent materials because they can absorb large amounts of aqueous fluid and desorb it under stress. One of the most critical parameters that limit the usefulness of SAP is its absorption capacity. Superabsorbent polymers can be used for water management and to renew arid and desert environments. This review demonstrates that superabsorbent materials can be beneficial to agriculture and the environment by reducing irrigation water consumption, improving fertilizer retention time in soil, decreasing plant mortality, and increasing plant growth. Nanotechnology could play a role in preparing superabsorbent nanocomposite materials by employing superabsorbent polymers. This article introduces superabsorbent/clay nanocomposites and the mechanochemical synthesis approach which are convenient and useful types of superabsorbent nanocomposites..

Keywords: Mechanochemical, Superabsorbent polymers, Nanotechnology, Agricultural, Nanocomposites, Nano clay.

Introduction

In nanotechnology, functional systems are engineered and reorganized by manipulating small molecules and atoms [1]. During the eighteenth and nineteenth centuries, medicine, food, pharmacology, and agriculture evolved into interdisciplinary with the potential to make drastic changes to all these fields [2]. As a result of population growth and its impact on agronomic practices and productivity, there is currently a lack of food supply in developing countries [3]–[5]. Numerous applications in agricultural fields can be enhanced with nanotechnology-based

Special Issue of the National Seminar of physics, Chemistry and their Applications “NSPCA’23”
March 6-7th, 2023, Mohamed El Bachir El Ibrahimi University, Bordj-Bou-Arreidj, Algeria.

devices [6], [7], from swiftly inspecting diseases to enhancing plant capacity to absorb minerals and promoting the molecular treatment of diseases [8]. Agricultural nanotechnology is growing from a theoretical perspective to a practical one [9]–[12]. An understanding of the experimental tool's capability to work at nanometric levels will create more opportunities for molecular and cellular biology research.

There are roughly 7 billion people on the planet, with about half of them living in Asia. Climate change effects on agriculture, such as storms, droughts, and floods, are leading to a severe food shortage in developing nations due to an increase in the proportion of those living in such areas [13]. Several biotic and abiotic factors similarly limit agricultural production, and insect pests, diseases, and weeds cause significant losses in potential agricultural production [14,15]. Mass production of nanomaterial-based pesticides and insecticides is being developed exclusively to manage insect pests and protect agricultural productivity by releasing nutrients and water molecules slowly, incorporating nanomaterial-mediated genetic material into plants to create insect pest-resistant varieties [16-19]. Precision farming products use these sensors exclusively [10,14]. Superabsorbent polymers (SAPs) are yet another type of polymer that is capable of retaining a great deal of water, usually more than ordinary sponges [20]. In most cases, they are composed of cross-connected polymeric organs. The polymer chains of many sorts of these materials have ionic associations to promote the diffusion of water within the system [21]. As a result, superabsorbent materials are known as hydrophilic building materials that can ingest large volumes of watery fluids in short periods. Then, they can desorb this liquid under anxiety conditions [22].

Currently, superabsorbent polymers have been considered increasingly for water handling, and also for the rehabilitation of parched and additionally abandoned environments [23], [24]. Presented evidence shows that superabsorbent materials can decrease water usage in both farming and environmental water systems. They can also change the time for maintaining compost in the soil, decrease the death rate for plants, and boost the growth rate for plants. Superabsorbent polymers can be adapted using nanotechnology to incorporate the work of nanomaterials [23], [24]. This can help in the development of superabsorbent nanocomposites. Due to their better performance and high surface

Special Issue of the National Seminar of physics, Chemistry and their Applications "NSPCA'23"
March 6-7th, 2023, Mohamed El Bachir El Ibrahimi University, Bordj-Bou-Arreridj, Algeria.

area utilization, nanoscale superabsorbent materials are used. Similarly, these materials decrease the amount of raw material required and improve productivity [22]. The field of horticulture can make extensive use of nanotechnology. Variety in precipitation sum, distribution, and quality directly affect yield creation in dryland areas. Under rainfed conditions, soil dampness plays the most vital role in affecting the second rice harvest after the first [25].

Hydrogels with super-absorbent properties may provide the most effective results in this area of investigation. The properties of polymeric superabsorbent materials have been experimented with at several scales, from full-scale to miniaturized to nanoscale [24]. Nanotechnology has been used as a perspective for changing the swelling capacity, gelatin quality, and mechanical and warm properties of super absorbents [24]. Many studies have been conducted on the use of nanotechnology to enhance the performance of superabsorbent polymers. The focus of the present article is to shed light on nanocomposites with superabsorbent polymers and their impact on the adjustment of SAP materials. The impact of nanoparticles and nano clay is explored in greater depth as well [4, 22, 26, 27].

A Classification of Saps

Based on their source, SAPs can be divided into two groups:

- Natural one: There are two types of natural polymers: polysaccharides-derived (such as cellulose, starch, alginate, and agarose) and polypeptides-derived (such as gelatin, collagen) are used extensively [28,29].
- Second one is the synthetic chemical types of plastic (vinyl acetate, polyacrylic acid, polyethylene glycol, methacrylic acid) that are developed from petrochemicals.

Like hydrogels, SAPs can be categorized based on several aspects. Depending on whether the cross-linked chains have an electrical charge located in them, SAPs may be divided into four groups [30]:

- ❖ Non-ionic type.
- ❖ Ionic (including anionic and cationic)
- ❖ Amphoteric electrolyte (ampholytic) containing both acidic and basic groups

- ❖ Zwitterionic (polybetaines) that contain both cationic and anionic groups for each repeating structural unit.

For instance, most SAP hydrogels on the market are anionic. In addition, SAPs, as well as their chemical structure, can be grouped into several categories, so the majority of standard SAPs fall into one of the following groups [30–32]:

- cross-linked polyacrylates and polyacrylamides
- Hydroxy cellulose copolymers with polyacrylonitrile or starch-polyacrylonitrile (PAN)
- Cross-linked maleic anhydride copolymers. Nevertheless, according to sources, SAPs can be classified into two categories, namely synthetic (petrochemical-derived) and natural. Hydrogels based on polysaccharides can be divided into two main groups, i.e. those based on polypeptides (proteins) and those based on polysaccharides. Most SAPs that are derived from natural sources include synthetic components as well, such as vinyl monomers being copolymerized with polysaccharides in graft copolymerization.

A word like "superabsorbent" sometimes means the most conventional form, that of anionic acrylic, which is a copolymer network derived from partially neutralized acetate acid (AA) or acetate amide (AM) [33].

Models of Statistical Analysis

A measurable model for polymer structure design assumes the polymer structure incorporates monomer units, based on probability guidelines. Literature has accounted for several factual computational models, including the recursive strategy [34], the piecing technique, and the production capacity strategy [35]. For the service of identical quantified depictions, the arbitrary cross-linking theory provides the following: (1) Carbon twofold bonds must be equivalent and autonomous; (2) no intramolecular cyclization is permitted; (3) permission of chain exchange or disproportionation; and (4) free energy changes. Transformative subordinate energy, cyclization with inexact treatment, and adjustment of the end components have all been accounted for [36, 37].

As shown in Figure 1, a free radical catalyzes polymerization through a connection likelihood design. A free radical cross-linking polymerization can be carried out under six different fortified conditions, as shown in figure 1 [21, 23, 30]. There are two properties of the reinforced conditions of a monomer unit: (1) the number of shapes of bonds between different monomers and (2) the Type(s) of fortified units. The mono vinyl acrylate monomer, as indicated in the figure, can be bonded in six different ways: not reacted, no bonds with different units, and one bond with another unit. Another monomer of acrylate; another crosslinker; two framed bonds, which may comprise two additional acrylate monomers; an acrylate and a crosslinker; or two crosslinkers[36].

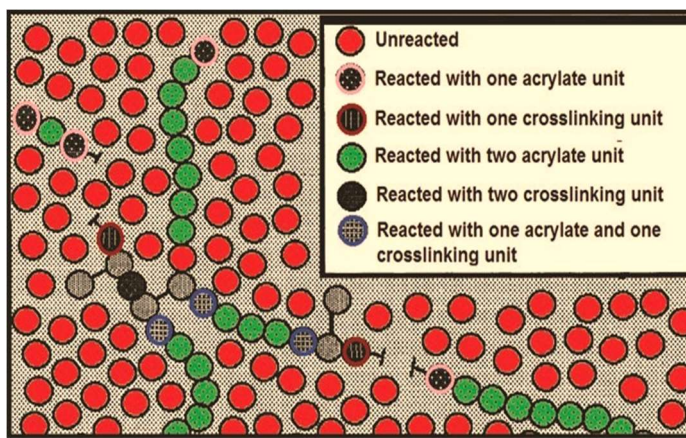


Figure 1. An acrylate monomer reacts with a radical free-radical crosslinking polymer during a polymerization process (modified from [36]).

Superabsorbent Clay Nanocomposites

According to Sigma-Aldrich Company, nano clays are dirt minerals that can be used to create polymer-clay nanocomposites having broad properties that can be applied to a wide variety of fields. Nano clay minerals are principally utilized as material components [23]. Montmorillonite is the most usually utilized as a part of these applications [27, 38]. Aluminosilicate layers are deposited on Montmorillonite's surface and are substituted with metal cations, forming stacks of about 10- μm high (Fig. 2).

Nanoparticles of polymer-earth nanocomposite are usually formed by scattering the stacks within the polymer framework. Nanocomposite layers are composed of nanoparticles

with a size of approximately 150 nanometers and a thickness of nm-thick clay layers entirely isolated from each other. Moreover, even at low nano clay stacking, Clays are polymers that dwell on a surface connected to nanocomposite, with polymer chains holding a majority of the weight share [23], [39].

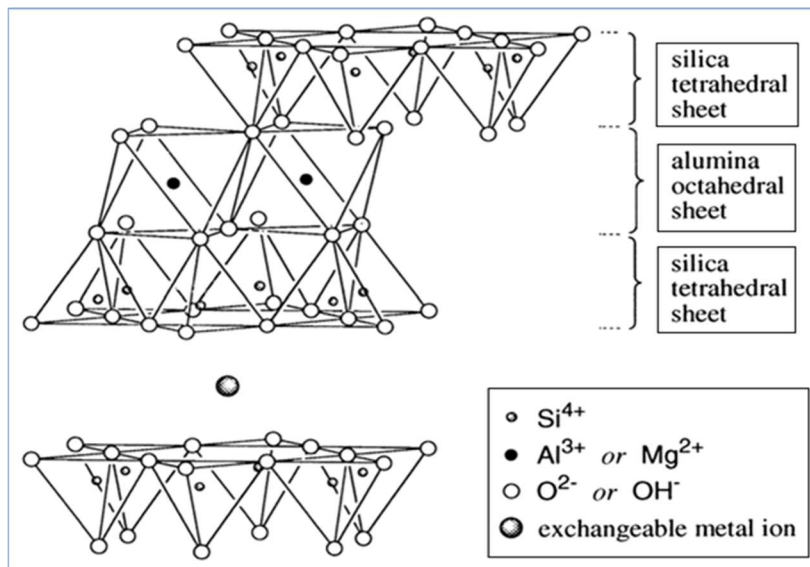


Figure 2. Structure of 2:1 clay mineral (modified from [40]).

The Montmorillonite mineral was discovered in Montmorillon, France, in 1847. In nature, bentonite is a key component of montmorillonite[40]. Montmorillonite is a substance that is mostly found in stones, which are extremely colloidal and plastic. Despite their similarity, kaolin clay particles and Bentonite particles differ on account of their thickness [23]. It is entirely possible that bentonite sodium or potassium salts could be sliced into thin plates with a thickness of 1 nm [41]. Montmorillonite is not the only mineral that may be found in bentonite. The mineral may also consist of crystalline quartz, feldspar, and cristobalite. A significant number of earth minerals-including Bentonite which is an amorphous, high-water-retaining material with thixotropic hydrogel properties, as well as high cation-trading capacity [42]. Dirt minerals may possess properties distinct from soil minerals, such as interstitial water and compatible cations in the interlayer [43].

As part of superabsorbent polymer alteration, montmorillonite (MMT) has been widely used. A superabsorbent made from MMT and NaAlg-g-poly(AA-co-AAm), Rashidzadeh et al. (2014) reported on compost-controlled discharge with the composite [44]. Incorporating montmorillonite into pure superabsorbent created the highly porous structure of Hyd/MMT/NPK, which enhanced water absorption of the composite [44].

Mechanisms Of Swelling in Superabsorbent Polymers

SAP materials swell for a variety of reasons. For swelling to occur, the following components have to be present for the last swelling limit (the amount of surface water that an SAP can hold once surface water has been removed by a centrifuge under free swelling conditions) [10, 22, 25, 43]. SAP polymer arrangements are depicted in Figure 3. Due to its hydrophilic nature and carboxylic acid gatherings (-COOH), SAP is a polymer spine. A polymer/dissolvable association results when watery arrangements are introduced to SAP; one of these is hydration, and another is hydrogen storage [25, 41, 43].

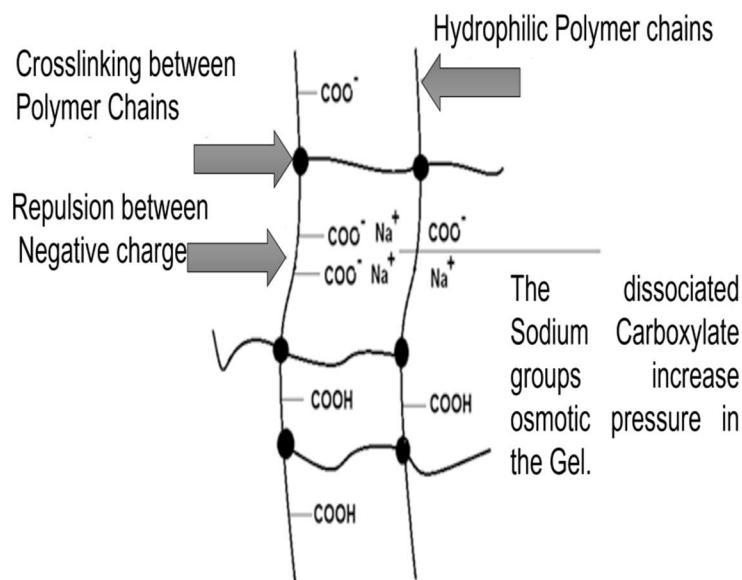


Figure3. Diagram of SAP network during swelling (modified from [10]).

Mechanochemical Synthesis of Superabsorbent Polymers

An efficient mechanochemical process involving the use of a ball mill can be applied for the successful synthesis of different

SAPs with a variety of applications fields such as perovskites like barium titanate[6], [7]. In the crystallographic analysis of the prepared powder, it was demonstrated that mechanically ground BaO and TiO₂ powder are converted fully into barium titanate after 90 minutes of milling [45]. Moreover, EDS analysis concluded that the tested samples contained only barium, oxygen, and titanate. Compared to aqueous suspensions, SAP suspensions of BaTiO₃ are more similar to the dry powder of barium titanate[45].

Agricultural Applications

Due to their ability to retain water, SAPs are used in agriculture as a water-saving material and soil conditioner [22]. Due to the expansion and contraction of polymeric particles during moisture cycles, SAPs enhance porosity in clayey soils. Plant growth was significantly moderated by SAP application in drought-stricken areas and irrigation deficit regions [46].

To attain water retention and controlled release properties, superabsorbents are used with fertilizers [47]. In addition to improving plant nutrition and water efficiency, this fertilizer and superabsorbent combination reduce evaporation losses and irrigation frequency [48]. In aquatic and terrestrial areas, SAPs are used to control pest infestations by preventing pests from escaping the granules. For this purpose, superabsorbents based on polyacrylates and polyacrylamides are mainly used. Other polysaccharides used in agriculture and horticulture include sodium alginate, ethyl cellulose, and chitosan [22]. In addition to controlling the release of herbicides, these hydrogels are soil conditioners that encourage plant growth as they are made of agar and starch [22].

Saps as A Source of Nutrition

In agricultural applications, nitrogen fertilizers are employed because it is an essential nutrient for plants [26]. Nitrogen fertilizers, such as urea (46%) are the most widely used [4]. By using slow-release fertilizers, it is possible to minimize nutrient losses observed due to surface runoff, leaching, and vaporization [26]. A slow-release fertilizer is advantageous beyond its reduction of nutrient losses because it provides a controlled and sustained supply of nutrients for a long time, allows the fertilizer to release

nutrients more efficiently, reduces the frequency of application, and reduces toxicity and overdose [22].

Hydrogel Sap as Water-Retention Agent

Due to their high-water absorption and retention abilities, superabsorbents conserve water, allowing soils to remain moist [44], [49]. To prevent the soil from drying out, the granules are mixed into it in prescribed amounts. Water is absorbed by the granules by swelling, and they release it as the soil dries by diffusion [22], [50]. This reduces evaporation and irrigation water loss [51]. In the process of absorbing water, the SAP grows and expands, and as a result, the soil becomes a lot more porous, which then increases oxygen availability to the roots. To promote plant growth in areas prone to drought, polyacrylate SAPs were used. The degradation of polyacrylate-based SAPs and the release of toxic chemicals has led to the development of new classes of environmentally friendly bio-based SAPs based on cellulose and starch [50].

Conclusions

Mechanochemical synthesis is an environmentally friendly, highly efficient, and time-saving, economical synthesis technique for creating new and efficient functional materials. This review provides a brief of recent advances in the use of superabsorbent polymers that can be used to replenish arid and desert settings and regulate water. Consequently, superabsorbent materials can benefit agriculture and the environment by using less water for irrigation, increasing the time fertilizer stays in the soil, lowering plant mortality, and promoting plant growth. Superabsorbent polymers could be used in nanotechnology to create superabsorbent nanocomposite materials.

References

- [1] H. Chhipa, “Nanofertilizers and nanopesticides for agriculture,” *Environ. Chem. Lett.*, vol. 15, no. 1, pp. 15–22, 2017, doi: 10.1007/s10311-016-0600-4.
- [2] E. AlShamaileh, A. E. Al-Rawajfeh, and M. Alrbaihat, “Mechanochemical Synthesis of Slow-release Fertilizers: A Review,” *Open Agric. J.*, vol. 12, no. 1, pp. 11–19, 2018,

doi: 10.2174/1874331501812010011.

- [3] P. Baláž, E. Godočiková, K. Iždinstý, J. Kováč, A. Šatka, and M. Achimovičová, “Mechanochemical dry synthesis of nanocrystalline semiconductors,” *2006 NSTI Nanotechnol. Conf. Trade Show - NSTI Nanotech 2006 Tech. Proc.*, vol. 1, no. 1, pp. 427–430, 2006.
- [4] E. M. AlShamaileh, A. E. Al-Rawajfeh, and M. R. Alrbaihat, “Solid-state mechanochemical synthesis of Kaolinite-Urea complexes for application as slow release fertilizer,” *J. Ecol. Eng.*, vol. 20, no. 9, pp. 267–276, 2019, doi: 10.12911/22998993/110962.
- [5] A. Said *et al.*, “Mechanochemical activation of phlogopite to directly produce slow-release potassium fertilizer,” *Appl. Clay Sci.*, vol. 165, no. August, pp. 77–81, 2018, doi: 10.1016/j.clay.2018.08.006.
- [6] M. R. Alrbaihat, A. E. Al-rawajfeh, and E. Alshamaileh, “A mechanochemical preparation , properties and kinetic study of kaolin – N , P fertilizers for agricultural applications **,” *J. Mech. Behav. Mater.*, vol. 30, pp. 265–271, 2021, doi: 10.1515/jmbm-2021-0028.
- [7] M. Alrbaihat, “A Review of Size Reduction techniques Using Mechanochemistry Approach,” *Egypt. J. Chem.*, vol. 65, no. 6, pp. 551–558, 2021, doi: 10.21608/ejchem.2021.105136.4848.
- [8] J. Huang *et al.*, “Biosynthesis of silver and gold nanoparticles by novel sundried Cinnamomum camphora leaf,” *Nanotechnology*, vol. 18, no. 10, 2007, doi: 10.1088/0957-4484/18/10/105104.
- [9] T. C. Madzokere, L. T. Murombo, and H. Chiririwa, “Nano-based slow releasing fertilizers for enhanced agricultural productivity,” *Mater. Today Proc.*, vol. 45, pp. 3709–3715, 2020, doi: 10.1016/j.matpr.2020.12.674.
- [10] R. Prasad, M. Kumar, and V. Kumar, “Nanotechnology: An agricultural paradigm,” *Nanotechnol. An Agric. Paradig.*, pp. 1–372, 2017, doi: 10.1007/978-981-10-4573-8.

- [11] H. Gupta, “Role of Nanocomposites in Agriculture,” *Nano Hybrids Compos.*, vol. 20, pp. 81–89, 2018, doi: 10.4028/www.scientific.net/nhc.20.81.
- [12] P. Subhaswaraj and B. Siddhardha, *Nanoemulsions for Antimicrobial and Anti-biofilm Applications*. 2020. doi: 10.1007/978-3-030-40337-9_15.
- [13] A. E. Al-rawajfeh, M. R. Alrbaihat, and M. Ehab, “Effects of Milling Time and Speed on Nutrient,” *Jordan J. Chem.*, vol. 15, no. 2, pp. 51–59, 2020, doi: 10.47014/15.2.1.
- [14] G. Dhaliwal, V. Jindal, and A. Dhawan, “Insect pest problems and crop losses: changing trends,” *Indian J. Ecol.*, vol. 37, no. 1, pp. 1–7, 2010, doi: 10.13140/RG.2.2.25753.47201.
- [15] M. R. Alrbaihat, *Agricultural Nano Fertilizers : Macronutrient*. Springer Nature Singapore, 2023. doi: 10.1007/978-981-19-7358-1.
- [16] H. peng Feng *et al.*, “Core-shell nanomaterials: Applications in energy storage and conversion,” *Adv. Colloid Interface Sci.*, vol. 267, pp. 26–46, 2019, doi: 10.1016/j.cis.2019.03.001.
- [17] K. Gajanan and S. N. Tijare, “Applications of nanomaterials,” *Mater. Today Proc.*, vol. 5, no. 1, pp. 1093–1096, 2018, doi: 10.1016/j.matpr.2017.11.187.
- [18] P. Baláž *et al.*, “Hallmarks of mechanochemistry: From nanoparticles to technology,” *Chem. Soc. Rev.*, vol. 42, no. 18, pp. 7571–7637, 2013, doi: 10.1039/c3cs35468g.
- [19] Y. Qian, C. Qin, M. Chen, and S. Lin, “Nanotechnology in soil remediation – applications vs. implications,” *Ecotoxicol. Environ. Saf.*, vol. 201, no. March, p. 110815, 2020, doi: 10.1016/j.ecoenv.2020.110815.
- [20] F. Esposito, M. A. Del Nobile, G. Mensitieri, and L. Nicolais, “Water sorption in cellulose-based hydrogels,” *J. Appl. Polym. Sci.*, vol. 60, no. 13, pp. 2403–2408, 1996, doi: 10.1002/(SICI)1097-4628(19960627)60:13<2403::AID-APP12>3.0.CO;2-5.

- [21] K. Mohana Raju, M. Padmanabha Raju, and Y. Murali Mohan, "Synthesis of superabsorbent copolymers as water manageable materials," *Polym. Int.*, vol. 52, no. 5, pp. 768–772, 2003, doi: 10.1002/pi.1145.
- [22] S. Behera and P. A. Mahanwar, "Superabsorbent polymers in agriculture and other applications: a review," *Polym. Technol. Mater.*, vol. 59, no. 4, pp. 341–356, 2020, doi: 10.1080/25740881.2019.1647239.
- [23] P. C. Lebaron, Z. Wang, and T. J. Pinnavaia, "Polymer-layered silicate nanocomposites: An overview," *Appl. Clay Sci.*, vol. 15, no. 1–2, pp. 11–29, 1999, doi: 10.1016/S0169-1317(99)00017-4.
- [24] V. P. Mahida and M. P. Patel, "Synthesis of new superabsorbent poly (NIPAAm/AA/N-allylisatin) nanohydrogel for effective removal of As(V) and Cd(II) toxic metal ions," *Chinese Chem. Lett.*, vol. 25, no. 4, pp. 601–604, 2014, doi: 10.1016/j.ccllet.2014.01.031.
- [25] G. Kumar Jatav, R. Mukhopadhyay, and N. De, "Characterization of Swelling Behaviour of Nanoclay Composite," *Int. J. Innov. Res. Sci. Eng. Technol.*, vol. 2, no. 5, 2013, [Online]. Available: www.ijirset.com
- [26] M. R. Alrbaihat, A. E. Al-rawajfeh, and E. Alshamaileh, "A mechanochemical preparation , properties and kinetic study of kaolin – N , P fertilizers for agricultural applications **," vol. 2021, pp. 265–271, 2021.
- [27] N. S. et al. . Nalini Sharma et al., "A Review on Changes in Fertilizers, From Coated Controlled Release Fertilizers (CRFs) to Nanocomposites of CRFs," *Int. J. Agric. Sci. Res.*, vol. 9, no. 2, pp. 53–74, 2019, doi: 10.24247/ijasrapr20197.
- [28] N. Thombare, S. Mishra, M. Z. Siddiqui, U. Jha, D. Singh, and G. R. Mahajan, "Design and development of guar gum based novel, superabsorbent and moisture retaining hydrogels for agricultural applications," *Carbohydr. Polym.*, vol. 185, pp. 169–178, 2018, doi: 10.1016/j.carbpol.2018.01.018.
- [29] R. Vundavalli, S. Vundavalli, M. Nakka, and D. S. Rao,

- “Biodegradable Nano-Hydrogels in Agricultural Farming - Alternative Source For Water Resources,” *Procedia Mater. Sci.*, vol. 10, no. Cnt 2014, pp. 548–554, 2015, doi: 10.1016/j.mspro.2015.06.005.
- [30] P. Klinpituksa and P. Kosaiyakanon, “Superabsorbent Polymer Based on Sodium Carboxymethyl Cellulose Grafted Polyacrylic Acid by Inverse Suspension Polymerization,” *Int. J. Polym. Sci.*, vol. 2017, 2017, doi: 10.1155/2017/3476921.
- [31] J. Zhang and A. Wang, “Study on superabsorbent composites. IX: Synthesis, characterization and swelling behaviors of polyacrylamide/clay composites based on various clays,” *React. Funct. Polym.*, vol. 67, no. 8, pp. 737–745, 2007, doi: 10.1016/j.reactfunctpolym.2007.05.001.
- [32] E. M. Ahmed, “Hydrogel: Preparation, characterization, and applications: A review,” *J. Adv. Res.*, vol. 6, no. 2, pp. 105–121, 2015, doi: 10.1016/j.jare.2013.07.006.
- [33] D. A. Kidwell, “Superabsorbent polymers-Media for the enzymatic detection of ethyl alcohol in urine,” *Anal. Biochem.*, vol. 182, no. 2, pp. 257–261, 1989, doi: 10.1016/0003-2697(89)90590-3.
- [34] N. A. Dotson, R. Galván, and C. W. Macosko, “Structural Development during Nonlinear Free-Radical Polymerizations,” *Macromolecules*, vol. 21, no. 8, pp. 2560–2568, 1988, doi: 10.1021/ma00186a041.
- [35] A. B. Scranton, J. Klier, and N. A. Peppas, “Statistical Analysis of Free-Radical Copolymerization/Cross-Linking Reactions Using Probability Generating Functions: Reaction Directionality and General Termination,” *Macromolecules*, vol. 24, no. 6, pp. 1412–1415, 1991, doi: 10.1021/ma00006a031.
- [36] A. B. Kinney and A. B. Scranton, “Formation and Structure of Cross-Linked Polyacrylates,” vol. i, pp. 2–26, 1994.
- [37] R. Poli, J. C. Gordon, and U. D. Arnold, “Formation and Structure of cross-linked polyacrylates,” vol. i, pp. 1518–1520, 1991.

- [38] Z. Qian, G. Hu, S. Zhang, and M. Yang, “Preparation and characterization of montmorillonite-silica nanocomposites: A sol-gel approach to modifying clay surfaces,” *Phys. B Condens. Matter*, vol. 403, no. 18, pp. 3231–3238, 2008, doi: 10.1016/j.physb.2008.04.008.
- [39] R. A. Vaia, K. D. Jandt, E. J. Kramer, and E. P. Giannelis, “Microstructural Evolution of Melt Intercalated Polymer-Organically Modified Layered Silicates Nanocomposites,” *Chem. Mater.*, vol. 8, no. 11, pp. 2628–2635, 1996, doi: 10.1021/cm960102h.
- [40] T. Shichi and K. Takagi, “Clay minerals as photochemical reaction fields. Journal of Photochemistry and Photobiology C,” *J. Photochem. Photobiol. C Photochem. Rev.*, vol. 1, no. September, pp. 113–130, 2000.
- [41] R. Wilson, N. Chandran, and S. Thomas, “Layered clay rubber composites,” *Key Eng. Mater.*, vol. 571, pp. 197–213, 2013, doi: 10.4028/www.scientific.net/KEM.571.197.
- [42] F. Slaty, H. Khoury, H. Rahier, and J. Wastiels, “Durability of alkali activated cement produced from kaolinitic clay,” *Appl. Clay Sci.*, vol. 104, pp. 229–237, 2015, doi: 10.1016/j.clay.2014.11.037.
- [43] F. Uddin, “Clays, nanoclays, and montmorillonite minerals,” *Metall. Mater. Trans. A Phys. Metall. Mater. Sci.*, vol. 39, no. 12, pp. 2804–2814, 2008, doi: 10.1007/s11661-008-9603-5.
- [44] A. Rashidzadeh and A. Olad, “Slow-released NPK fertilizer encapsulated by NaAlg-g-poly(AA-co-AAm)/MMT superabsorbent nanocomposite,” *Carbohydr. Polym.*, vol. 114, pp. 269–278, 2014, doi: 10.1016/j.carbpol.2014.08.010.
- [45] S. Kudłacik-Kramarczyk *et al.*, “Mechanochemical synthesis of BaTiO₃ powders and evaluation of their acrylic dispersions,” *Materials (Basel)*, vol. 13, no. 15, 2020, doi: 10.3390/MA13153275.
- [46] M. Sayyari and F. Ghanbari, “Effects of Super Absorbent Polymer A200 on the Growth, Yield and Some Physiological Responses in Sweet Pepper (*Capsicum*

- Annuum L.) Under Various Irrigation Regimes,” *Int. J. Agric. Food Res.*, vol. 1, no. 1, pp. 1–11, 2012, doi: 10.24102/ijafr.v1i1.123.
- [47] B. Ni, M. Liu, and S. Lü, “Multifunctional slow-release urea fertilizer from ethylcellulose and superabsorbent coated formulations,” *Chem. Eng. J.*, vol. 155, no. 3, pp. 892–898, 2009, doi: 10.1016/j.cej.2009.08.025.
- [48] L. Wu and M. Liu, “Preparation and properties of chitosan-coated NPK compound fertilizer with controlled-release and water-retention,” *Carbohydr. Polym.*, vol. 72, no. 2, pp. 240–247, 2008, doi: 10.1016/j.carbpol.2007.08.020.
- [49] S. Kiatkamjornwong, “Superabsorbent Polymers and Superabsorbent Polymer Composites,” *ScienceAsia*, vol. 33, no. 1, pp. 39–43, 2007, doi: 10.2306/scienceasia1513-1874.2007.33(s1).039.
- [50] G. Cannazza, A. Cataldo, E. de Benedetto, C. Demitri, M. Madaghiele, and A. Sannino, “Experimental assessment of the use of a novel superabsorbent polymer (SAP) for the optimization of water consumption in agricultural irrigation process,” *Water (Switzerland)*, vol. 6, no. 7, pp. 2056–2069, 2014, doi: 10.3390/w6072056.
- [51] B. Azeem, K. Kushaari, Z. B. Man, A. Basit, and T. H. Thanh, “Review on materials & methods to produce controlled release coated urea fertilizer,” *J. Control. Release*, vol. 181, no. 1, pp. 11–21, 2014, doi: 10.1016/j.jconrel.2014.02.020.



Thermal/optical study and characterization of a MCP doped with In_2O_3 and AlCl_3 for solar use

Maifi Lyes^{1,3*}, Agroui Kamel¹, Hioual Ouided^{2,3} and Chari Abdelhamid³

¹ Research Center on Semiconductor Technology for Energetic, TESE-CRTSE, 2 BD Frantz Fanon, 7 merveilles, POB 140, Algiers, Algeria,

² Mathematics and Computer Science Department Abbes Laghrou University Khenchela, Algeria,

³ Thermodynamic laboratory and surface treatment of materials Physics Department Mentouri University Constantine, Algeria

* Corresponding author: Tel./Fax: +213670328648; E-mail address: maifi.lyes@crtse.dz
DOI: <https://doi.org/10.58452/jpcr.v2i2.167>

Article history

Received May 04, 2023

Accepted for publication December 03, 2023

Abstract

Thermal insulation is one of the major problems of building comfort. One of the solutions proposed is the use of the latent heat of phase change materials to evacuate the external heat in order to keep it at an adequate temperature in the chamber. In this work, we use the latent heat of a MCP type $\text{C}_{25}\text{H}_{52}$ pure and doped with two types of dopant In_2O_3 and AlCl_3 for the climatic application. We study the effect of dopant nature and doping rate on phase change time, latent heat and mass loss. To improve this time we doped our material with In_2O_3 , and AlCl_3 . The study consists in monitoring the evolution of the phase change time, the flow of the latent heat and the loss of the mass according to the nature of the dopant and the doping rate. A study of the DSC, ATG, FTIR and PL characterization is presented. The study showed that the best dopant for solar insulation is AlCl_3 doping.

Keywords: MCP, AlCl_3 , PL, FTIR, DSC.

1. Introduction

Several works are carried out, on thermal insulation of the building in a material with phase change, either by the improvement of the cooling thanks to the natural or forced convection, or by the absorption of the excess of the external heat, we can quote:

In The work of H. Manz et al. (1997) [1], they proposed a wall of phase change material, the hydrated salt (melting temperature of 26.5°C) and a TIM. The phase change material transmits the visible spectrum of solar radiation, producing natural light. It is contained in glass bricks. The part of solar radiation in the infrared is stored by the latent heat during the melting of phase change material.

A transparent insulating material is added to the extra thickness of the wall to remedy the losses observed in other types of storage walls.

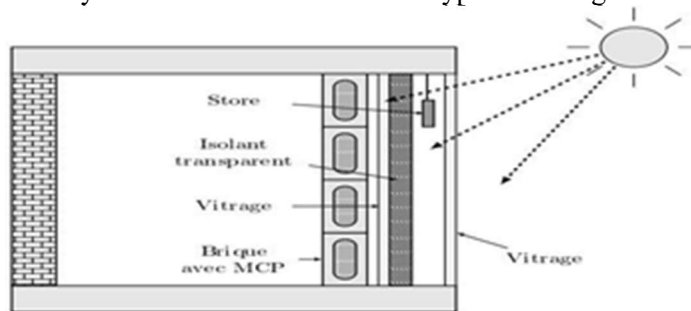


Figure 1. Wall with MCP and TIM.

The authors developed a one-dimensional numerical model coupling conduction and radiation, and compared their numerical results to experiments, using data from a single brick in the middle of the wall in order to avoid edge effects.

In 2004, Mohamed M. Farid et al. [2] present a detailed work of systems using phase change materials (PCM) to store thermal energy in building applications. This review presents the different methods of incorporating phase change materials within the envelope. The conclusion of this work is that the introduction of phase change materials in the building envelope can minimize temperature fluctuations by using solar energy.

An active system was used by Vineet Veer Tyagi and D. Buddhi in 2007 [3] to offload the electrical network during periods of peak consumption, electrical energy is therefore preferentially used during off-peak hours when it is at a lower cost to be stored as latent heat. The principle is to melt or solidify an PCM during off-peak hours in order to solidify it during peak hours and thus restore the heat to the part.

Special Issue of the National Seminar of physics, Chemistry and their Applications "NSPCA'23"

March 6-7th, 2023, Mohamed El Bachir El Ibrahimi University, Bordj-Bou-Arreridj, Algeria.

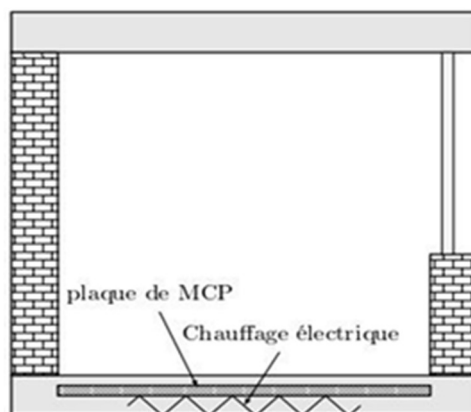


Figure 2. Diagram of underfloor heating

In 2009 Zhu, Ma and Wang [4] focused on work on the dynamic characterization of the behavior of PCMs, necessary to optimize their use on the performance of buildings incorporating phase change materials. The conclusion of this work is that the use of phase change materials can have positive consequences on the energy performance of a building but the heat transfer is sometimes insufficient and the selection of a PCM must be made according to the climate. In which the building is located. However, the studies remain insufficient to correctly predict the possible gains.

The purpose of using these materials is to extend the duration of thermal stability (constant temperature) on the wall beyond 8 hours, which corresponds to the time of sunshine. Unfortunately, paraffin has a low thermal conductivity which does not allow good heat transfer between the material and the ambient air [1-6]. The solution to this problem is the doping of paraffin with fine oxides of high thermal conductivity [5-8]. In recent years, with the development of nanomaterials, studies have begun to improve the thermal conductivity of the base material. by adding nanoparticles, called “nanomaterials”[7-13].

In this paper, we are interested in the influence of doping rate on the phase change time and the latent heat of the material in time and temperature. A thermal characterization (DSC, ATG), optical (PL), spectroscopy (FTIR) and morphology of our materials are studied.

2. Method

In this work, we used a $C_{25}H_{52}$ type paraffin which was doped with In_2O_3 and $AlCl_3$ in the range of 0 and 30% atomic. The material was heated to boiling temperature to obtain its liquid phase using a STUART CC62 hot plate equipped with a STUART SCT1 controller allowing the measurement of temperature as a function of time. The doping agents used are RIEDEL DE HAEM brand In_2O_3 and PRESI brand powdered $AlCl_3$.

Table 1. Characteristics of dopants and MCP

	Density g.cm ⁻³	Melting temperature °C	Molar mass g.mol ⁻¹	Boiling temperature °C
In_2O_3	2.44-2.48 g.cm ⁻³	190°Cà 2.5 atm	133.34 g.mol ⁻¹	182,7 °Cà 752 mmHg
$AlCl_3$	3.97 g.cm ⁻³	2050°C	102 g.mol ⁻¹	2980°C
MCP	0.9 g.cm ⁻³	50-59°C	404 g.mol ⁻¹	190°C

3. Results

3.1 Thermal characterization

Figures 5 and 6 shows the influence of doping rate on time as a function of paraffin temperature during the phase change for the two types of dopants.

It is clearly observed that:

The temperature is constant during the phase change period.

The phase change time increases with the doping rate regardless of the type of dopant.

The phase change time evolution is much better for $AlCl_3$ compared to In_2O_3 .

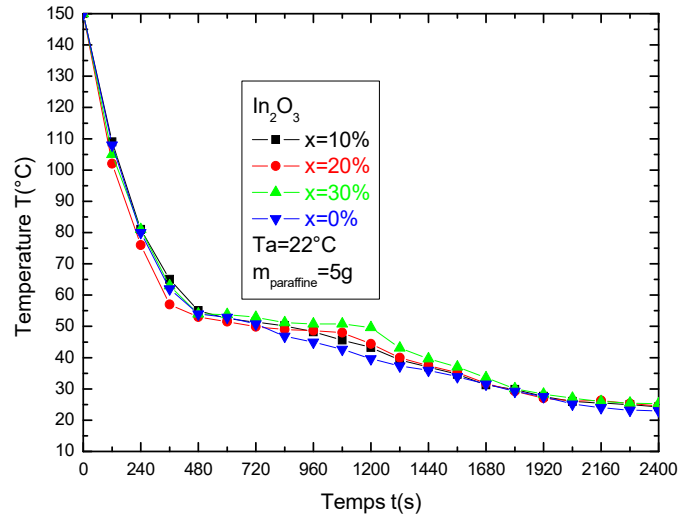


Figure 5. The variation of temperature as a function of time of In_2O_3 for different doping rates of a mass of 5 g.

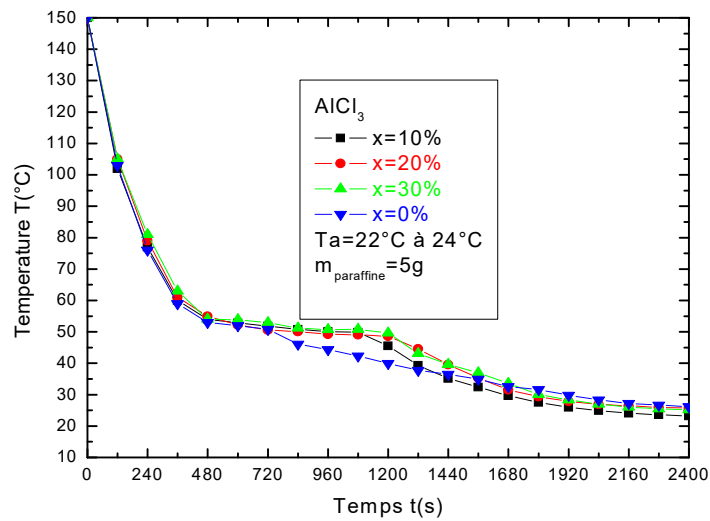


Figure 6. The variation of temperature as a function of time of AlCl_3 for different doping rates of a mass of 5 g.

3.2 DSC characterization

The measurement of the heat flow as a function of the temperature of the oven is carried out from the zero temperature 0°C up to the temperature 100°C, with a heating rate equal to 5°C/min.

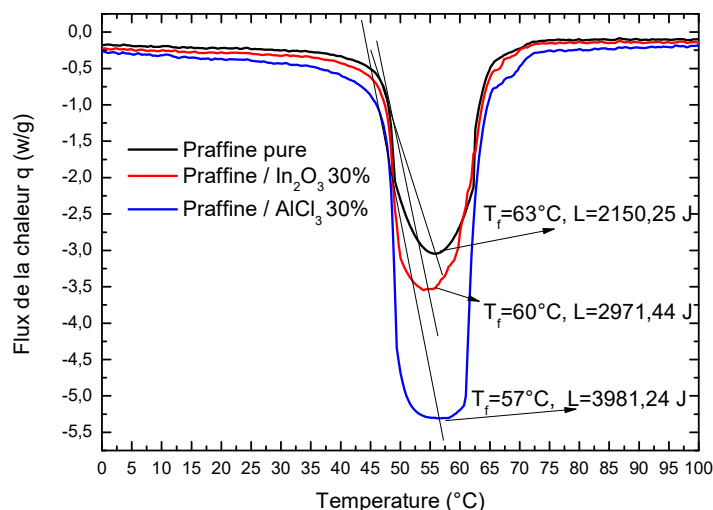


Figure 7. DSC $q=f(T)$ curves of pure paraffin, doped with In_2O_3 and AlCl_3 (30%)

This curve represents the heat flux changes of pure paraffin and paraffin doped with In_2O_3 and AlCl_3 (30%) and as a function of oven temperature. It is observed that the material begins to absorb heat at the temperature of the beginning of the phase change (45°C, 8.1J/g), where and this is maximum, and then returns to the zero point when it is completely transformed into liquid. The latent heat increases with increasing doping rate for all types of dopants and it is maximum for AlCl_3 .

The thermal measurement of our material shows that the phase change time enters into the characterization of the heat transfer between the material and the surface of the wall. This time is proportional to the amount of heat transferred and is greater as the doping rate is high.

These results show that there is a relationship between the thermal conductivity and the latent heat when the thermal conductivity is increased with the injection of the nanoparticles, the latent heat increases and increases the phase change time, this study confirms the results obtained on the phase change time calculation.

3.3 Optical characterization

This curve represents the influence of the doping rate on the intensity as a function of the wavelength. It is shown that the intensity decreases with increasing doping rate, which means that both dopants decrease the intensity of the material.

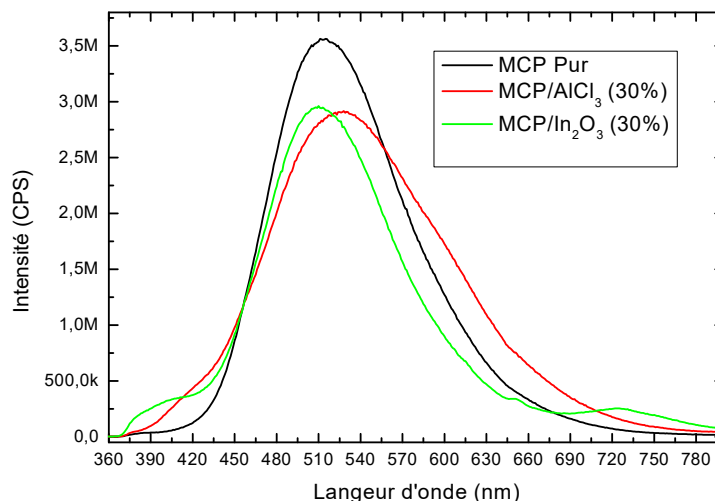


Figure 9. Pure paraffin photoluminescence, paraffin doped with In_2O_3 and AlCl_3 30%

We observe in our figure of paraffin/ AlCl_3 , In_2O_3 and a broad band of absorbance, and this band is very important increases for the doping by AlCl_3 , therefore our material doped by AlCl_3 appears as a suitable material with many favorable properties for solar and nuclear applications. Our spectrum of MCP/ In_2O_3 , exhibit two bands of luminescence, a band of short wavelength, located near the absorption edge of the crystal, i.e. the edge luminescence, and another wide band of long wavelength, the maximum of which is generally located in the 430-800 nm spectral range. A strong emission is observed at 450-720 nm associated with the presence of surface defects on the nanoparticles for the two types of dopants. At the same time, an emission peak of 410 nm when increasing the doping rate by 20% for MCP/ In_2O_3 nanoparticles gives a gap of 3.1 eV.

5. Conclusion

In this work, we show that the use of phase change materials with high thermal conductivity is a solution for solar cooling and storing energy. The injection of high thermal conductivity nanoparticles of In_2O_3 and AlCl_3 improves its thermal conductivity. To see the influence of the doping effect of In_2O_3 and AlCl_3 on the paraffin, thermal, optical and spectroscopic characterizations are presented. It is concluded that for all the dopants the doping improves the phase change time and the latent heat. The experimental results show that the use of doped paraffin on the walls of buildings is an effective solution for solar cooling and it is very important in the case of AlCl_3 doping.

References

- [1] H. Manz, P. Egolf, P. Suter, and A. Goetzberger, "TIM-PCM external wall system for solar space heating and day lighting," *Solar Energy*, Vol.61.369–379, 1997. [https://doi.org/10.1016/S0038-092X\(97\)00086-8](https://doi.org/10.1016/S0038-092X(97)00086-8).
- [2] Khudair, A.M. et M.M Farid « A review on phase change energy storage : materials and applications. *Energy Conversion and Management*, Vol.45.1597-1675, 2004.<https://doi.org/10.1016/j.enconman.2003.09.015>
- [3] V. V. Tyagi and D. Buddhi, "PCM thermal storage in buildings: state of the art," *Renewable and Sustainable Energy Reviews*, Vol.11. 1146–1166, 2007.
- [4] Zhu, Na, Zhenjun Ma et Shengwei Wang « Dynamic characteristics and energy performance of buildings using phase change materials: A review ». *Energy conversion and Management*, Vol. 50(10).316-318, 2009.<https://doi.org/10.1016/j.enconman.2009.08.019>.
- [5] A. Gontard, K. Gryska, L. Lallemand « Amélioration de la conductivité thermique de matériau à changement de phase », Université de Pau des pays de l'Adour 2012.
- [6] Zalba B., Mari'n J.M., Cabeza L.F., and Mehling H. « Review on thermal energy storage with phase change : materials, heat transfer analysis and applications» *Appl Therm Eng.* 2003 ; 23 :251-83. » *Appl Therm Eng.* 2003 ; 23 :251-83. [https://doi.org/10.1016/S1359-4311\(02\)00192-8](https://doi.org/10.1016/S1359-4311(02)00192-8)
- [7] A Benmoussa, L Rahmani, Numerical Analysis of thermal behavior in agitated vessel with Non-Newtonian fluid, *The International Journal of Multiphysics*, 2018, 12(3), 209-220. <https://doi.org/10.21152/1750-9548.12.3.209>
- [8] M Shibuta, H Hamashima, S Itoh, Numerical Simulation and Experiment for Underwater Shock Wave in Newly Designed Pressure Vessel, *The International Journal of Multiphysics*, 2010, 4(3), 241-258. <https://doi.org/10.1260/1750-9548.4.3.241>
- [9] Bruno BINET « Etude de la fusion dans des enceintes munies de sources de chaleur discrètes ». Sherbrooke (Québec), CANADA Novembre 1998.
- [10] J. P. Bédécarrats, Etude des transformations des matériaux changement de phases encapsulés destinés au stockage du froid. Thèse, Université de Pau et des Pays de l'Adour, Pau, 1993.

Special Issue of the National Seminar of physics, Chemistry and their Applications "NSPCA'23"

March 6-7th, 2023, Mohamed El Bachir El Ibrahim University, Bordj-Bou-Arreidj, Algeria.

- [11] A. Benmansour et M.A. Hamdan « Simulation du Stockage de l'Energie Thermique dans un Lit Fixe de Sphères Contenant un Matériau à Changement de Phase », Département de Chimie, Faculté des Sciences, Université des Sciences et de la Technologie Mohamed Boudiaf d'Oran, 2001.
- [12] MaifiLyes, KerbacheTahar, HioualOuided, Chari Abdelhamid, Effect of air channel depth and mass flow rate on the efficiency of hybrid thermal - Photovoltaic sensor, *The International Journal of Multiphysics*, 2018, 12(2), 147-167. <https://doi.org/10.21152/1750-9548.12.2.147>.
- [13]HioualOuided, Laskri M Tayeb, HemamSofianeMounine, HioualOuassila, MaifiLyes, Towards An Implementation of A Modified Static Load Balancing Algorithm To Minimize Execution Time, *Recent Patents on Computer Science*, Volume 12, Number 1, 2019, pp. 69-74(6), DOI: <https://doi.org/10.2174/2213275911666181022113733>

- **Aims and scope:** The Journal of Physical and Chemical Research is an English, French or arabic language peer-reviewed half yearly publication, open access journal, free of charges. The journal edited by: Laboratory of Materials Physics, Radiation and Nanostructures (LPMRN), Faculty of Sciences and Technology, Mohamed El Bachir El Ibrahimi University, Bordj-Bou-Arredj, Algeria. It publishes regular research papers (articles) and short communications. The motivation for this journal is to encourage scientists to publish their experimental and theoretical results in the field of Physical, Chemical and the related subjects. Papers previously published elsewhere cannot be accepted for the journal. Submission must be done at the following email address: jpcr@univ-bba.dz . The acceptance for publication lies on the recommendations of at least two ad hoc referees, and of the editorial board, if necessary.

- **Topics:**

- Astrophysics and astroparticles
- Atomic and molecular physics
- Biological physics
- Chemical physics and physical chemistry
- Computational science
- Condensed matter
- Fluids and fluid dynamics
- Gravitation and cosmology
- Instrumentation and measurement
- Mathematical physics
- Medical physics
- Nuclear physics
- Optics, quantum optics and lasers
- Particle physics and field theory
- Semiconductors
- Soft matter, liquids and polymers
- Statistical physics and nonlinear systems
- Surfaces, interfaces and thin films
- Thermodynamics
- Statistical Mechanics and Thermodynamics
- Molecular Spectroscopy
- Quantum Chemistry
- Computational Chemistry
- Physical Chemistry of Life Sciences
- Surface Chemistry
- Catalysis
- Physical Chemistry of Electrochemistry
- Kinetics
- Nanochemistry and Nanophysics
- Liquid Crystals
- Ionic Liquid
- Photochemistry
- Experimental article of Physical chemistry
- Mathematical Chemistry

First Legal Deposit: December, 2023